ELSEVIER

Modeling CO_2 chemistry, $\delta^{13}C$, and oxidation of organic carbon and methane in sediment porewater: Implications for paleo-proxies in benthic foraminifera

Richard E. Zeebe *

School of Ocean and Earth Science and Technology, Department of Oceanography, University of Hawaii at Manoa, 1000 Pope Road, MSB 504, Honolulu, HI 96822, USA

Abstract

I present a numerical diffusion–advection-reaction model to simulate CO_2 chemistry, $\delta^{13}C$, and oxidation of organic carbon and methane in sediment porewater. The model takes into account detailed reaction kinetics of dissolved CO_2 compounds, H_2O, H^+, OH^-, boron and sulfide compounds. These reactions are usually assumed to be in local equilibrium, which is shown to be a good approximation in most cases. The model also includes a diffusive boundary layer across which chemical species are transported between bottom water and the sediment–water interface. While chemical concentrations and $\delta^{13}C_{TCO_2}$ at these locations are frequently assumed equal, I demonstrate that they can be quite different. In this case, shells of benthic foraminifera do not reflect the desired properties of bottom water, even for species living at the sediment–water interface ($z = 0$ cm). Environmental conditions recorded in their shells are strongly influenced by processes occurring within the sediment. The model is then applied to settings in the Santa Barbara Basin and at Hydrate Ridge (Cascadia Margin), locations of strong organic carbon and methane oxidation. In contrast to earlier studies, I show that a limited contribution of methane-derived carbon to porewater TCO_2 in the Santa Barbara Basin cannot be ruled out. Simulation of methane venting shows that at oxidation rates greater than $F_{CH_4} \sim 50$ µmol cm^{-2} y^{-1}, the $\delta^{13}C$ of porewater TCO_2 at $z > 1$ cm is depleted by more than 15‰ relative to bottom water. Depletions of this magnitude have not been observed in living benthic foraminifera, even at methane vents with much higher oxidation rates. This suggests that foraminifera at these sites either calcify at very shallow sediment depth or during times when oxidation rates are much lower than ~ 50 µmol cm^{-2} y^{-1}.
© 2007 Elsevier Ltd. All rights reserved.

1. INTRODUCTION

Carbon fluxes to and from marine sediments are important in regulating inventories of Earth's surficial carbon reservoirs (for review, see Morse and Mackenzie, 1990; Mackenzie and Lerman, 2006). Key to reconstructing and predicting those fluxes is a fundamental understanding of sediment $CaCO_3$ accumulation and dissolution, for instance, driven by bottom water undersaturation and/or organic carbon respiration (e.g. Berner, 1980; Keir, 1982; Boudreau, 1987; Archer, 1991; Martin and Sayles, 1996). For example, projections of future fossil fuel neutralization depend on model descriptions of $CaCO_3$ dissolution in deep-sea sediments (Broecker and Takahashi, 1977; Sundquist, 1986; Archer et al., 1998). More recently, methane hydrate reservoirs in marine sediments have received strong attention because of their relevance to climate (e.g. Kvenvolden, 1988; Gornitz and Fung, 1994; Buffett and Archer, 2004). At productive continental margins, large methane and carbon fluxes have been observed, often associated with anaerobic oxidation of methane (AOM) by microbial consortia (e.g. Wallmann et al., 1997; Suess et al., 1999; Boetius et al., 2000; Luff and Wallmann, 2003). A quantitative understanding of these processes requires theoretical

* Fax: +1 808 956 7112.
E-mail address: zeebe@hawaii.edu

approaches, including numerical modeling of sediment porewater chemistry.

In addition to the relevance of sediments to the carbon cycle, marine sediments also provide a habitat for benthic organisms such as foraminifera. The fossil shells of benthic foraminifera are widely used in paleoceanography as indicators of past ocean conditions. For instance, their stable carbon and oxygen isotope composition ($\delta^{13}C$ and $\delta^{18}O$) is used as proxies for water mass distribution, temperature and density, and as a stratigraphic tool (e.g. Skinner and Shackleton, 2005; Curry and Oppo, 2005; Lynch-Stieglitz et al., 2006). Proxies to reconstruct the deep ocean's CO_2 chemistry (e.g. pH and $[CO_3^{2-}]$) are also much desired because they could resolve the mystery of glacial–interglacial changes in atmospheric CO_2 (e.g. Sigman and Boyle, 2000) or help in constraining past atmospheric CO_2 levels on longer time scales (e.g. Tyrrell and Zeebe, 2004). For example, the stable boron isotope composition ($\delta^{11}B$) of benthic foraminifera has been used to reconstruct past deep-water pH (Sanyal et al., 1995; Hönisch et al., 2006), while past deep-sea carbonate ion concentrations ($[CO_3^{2-}]$) and pH have been inferred from Zn/Ca and B/Ca ratios (Marchitto et al., 2002; Yu and Elderfield, 2006).

One fundamental assumption underlying the above proxies is that the tests of fossil foraminifera reflect ocean bottom water properties at the time the organism built its shell. Test of several critical aspects of this assumption will be presented in this paper. Theoretical progress has recently been made on proxy validation in planktonic foraminifera (Wolf-Gladrow et al., 1999; Zeebe et al., 1999a, 2003). Similar progress, which builds on previous work (e.g. McCorkle et al., 1985; Bernhard and Sen Gupta, 1999; Hintz et al., 2004) is likewise desirable for benthic foraminifera. One goal of the current paper is to advance progress towards this objective.

This study also aims to elucidate the effects of the oxidation of organic carbon (C_{org}) and methane (CH_4) on porewater and foraminiferal $\delta^{13}C$. For example, the proposed dissociation of methane hydrate in sediments of the Santa Barbara Basin is controversial (e.g. Kennett et al., 2000; Stott et al., 2002). The debate involves porewater TCO_2 and $\delta^{13}C_{TCO_2}$ data, based on which C_{org} has been identified as the sole source for porewater ^{13}C depletions. Using a new model, I will arrive at a different conclusion. At Hydrate Ridge (Cascadia Margin) anaerobic oxidation of methane produces very light porewater $\delta^{13}C_{TCO_2}$ values (Torres et al., 2003). However, such strong ^{13}C depletions have not been found in the shells of live benthic foraminifera from these sites (Torres et al., 2003; Hill et al., 2004). In order to evaluate these observations, I will provide a theoretical analysis of the relevant chemical fluxes and stable carbon isotope partitioning.

In the following, a new numerical model will be introduced (Section 2). New features, such as chemical kinetics vs. equilibrium, will be described in detail (Sections 2.2 and 3). Model results describing the effects of $CaCO_3$ dissolution and organic carbon respiration on the chemistry across the diffusive boundary layer will be presented in Section 4. A general description of the effect of organic carbon respiration on porewater chemistry and $\delta^{13}C$ of dissolved

CO_2 species will be given in Section 5. Specific applications of the model to carbon oxidation in the Santa Barbara Basin and methane oxidation at Hydrate Ridge are presented in Section 6. Finally, the implications of the present study for sediment modeling, carbon and methane cycling, and for paleo-proxies in benthic foraminifera are summarized in Section 7.

2. THE MODEL

The numerical model is based on solving transport-reaction equations for the various solutes, including the effects of diffusion, advection, and reaction—an approach similar to those of previous studies (cf. Berner, 1980; Boudreau, 1987; Archer, 1991; Martin and Sayles, 1996). However, as explained below, the current model takes detailed reaction kinetics into account and simultaneously solves steady-state equations for 16 chemical species (CO_2, HCO_3^-, CO_3^{2-}, H^+, OH^-, $B(OH)_3$, $B(OH)_4^-$, Ca^{2+}, O_2, $^{13}CO_2$, $H^{13}CO_3^-$, $^{13}CO_3^{2-}$, CH_4, SO_4^{2-}, H_2S, and HS^-). A general differential equation for a solute reads:

$$0 = \frac{\partial(\phi c_i)}{\partial t} = \frac{\partial}{\partial z}\left(\phi \, D_i \, \frac{\partial c_i}{\partial z}\right) - \frac{\partial(\phi w c_i)}{\partial z} + \phi R_i \qquad (1)$$

where c_i represents the concentration of chemical compound i, ϕ is the porosity, t is time, z is depth, D_i is the solute diffusion coefficient in the sediment (seawater coefficient corrected for tortuosity), and w is the porewater advection velocity (for units and other variables, see Table 1). The source/sink term due to chemical reactions, R_i, is specific for each compound and includes kinetic reaction terms (Section 2.2), dissolution and precipitation terms, and expressions for C_{org} and methane oxidation. For example, C_{org} respiration and $CaCO_3$ dissolution are included as source and sink terms in the solute equations for CO_2/O_2 and CO_3^{2-}/Ca^{2+}, respectively. The terms for $CaCO_3$ dissolution/precipitation and the oxidation terms are explained below (Sections 2.3, 2.5, and 2.6).

The resulting second-order differential equations with boundary conditions were solved using a relaxation method (solvde) from numerical recipes in C (Press et al., 1992). Briefly, the differential equations are replaced by approximate finite-difference equations on a grid of points that span the model domain. The method then determines the solution by starting with an educated guess and iteratively improving it until a problem-specific error is smaller than a prescribed margin. The equidistant grid spacing, Δz, was varied according to the numerical experiment; in cases with strong spatial gradients, Δz was reduced to 0.02 mm.

2.1. Porosity and diffusion coefficients

Observations show that porosity usually decreases with the $CaCO_3$ fraction f_c (e.g. Mayer, 1991; Herbert and Mayer, 1991). That is, sediment with high $CaCO_3$ content has a higher concentration of total solids per unit volume than low carbonate sediment. The relationship between porosity and f_c for a sediment layer composed of $CaCO_3$, clay, and porewater is given by (Zeebe and Zachos, in press):

Table 1
List of symbols and abbreviations used

Symbol	Description	Unit
a	Conversion factor mol C to kg $CaCO_3$	$kg\,mol^{-1}$
AOM	Anaerobic Oxidation of Methane	—
c_i	Solute concentration	$mol\,m^{-3}$
c_s	$[CO_3^{2-}]$ at $CaCO_3$ saturation	$mol\,m^{-3}$
C_{org}	Organic carbon	—
D	Diffusion coefficient	$m^2\,s^{-1}$
f_c	$CaCO_3$ solid dry weight fraction	$g\,g^{-1}$
$F_{C_{org}}$	Depth-integrated C_{org} respiration rate	$\mu mol\,cm^{-2}\,y^{-1}$
F_{CH_4}	Depth-integrated AOM rate	$\mu mol\,cm^{-2}\,y^{-1}$
k_{cs}	AOM rate constant	$dm^3\,mol^{-1}\,y^{-1}$
k_d	Dissolution rate constant	d^{-1}
k_p	Precipitation rate constant	$mol\,m^{-3}\,s^{-1}$
K_{sp}^*	Solubility product	$mol^2\,kg^{-2}$
l	Length scale of model domain	m
$l_{\nabla c}$	Length scale of spatial gradient	m
n	Dissolution reaction order	—
n_p	Precipitation reaction order	—
pH_t	pH on total scale	—
R_i	Source/sink term of chemical reactions	$mol\,m^{-3}\,s^{-1}$
$R_{C_{org}}$	C_{org} respiration term	$mol\,m^{-3}\,s^{-1}$
R_d	$CaCO_3$ dissolution term	$mol\,m^{-3}\,s^{-1}$
R_p	$CaCO_3$ precipitation term	$mol\,m^{-3}\,s^{-1}$
s	$1 - c/c_s$	—
t	Time	s
TA	Total alkalinity, $TA = [HCO_3^-] + 2[CO_3^{2-}] \ldots + [OH^-] - [H^+] + [B(OH)_4^-] + [HS^-]$	$mol\,kg^{-1}$
TCO_2	Total dissolved inorganic carbon, $TCO_2 = [CO_2] + [HCO_3^-] + [CO_3^{2-}]$	$mol\,kg^{-1}$
w	Porewater advection velocity	$m\,s^{-1}$
z	Depth	m
z_g	$1/e$-depth C_{org} respiration	m
z_ϕ	$1/e$-depth porosity	m
$z_{s/2}$	Depth at which s drops to 50%	m
Δz	Grid spacing	m
$\delta^{13}C_{CH_4}$	$\delta^{13}C$ of CH_4	‰
$\delta^{13}C_{CO_2}$	$\delta^{13}C$ of dissolved CO_2	‰
$\delta^{13}C_{TCO_2}$	$\delta^{13}C$ of TCO_2	‰
$\delta^{13}C_{res}$	$\delta^{13}C$ of respired CO_2	‰
γ	$\zeta\,f_c/c_s/\phi/D$	m^{-2}
ζ	$k_d\,(1-\phi)\,\rho/a$	$mol\,m^{-3}\,s^{-1}$
λ	Reacto-diffusive length scale	m
ρ	Solid density	$kg\,m^{-3}$
τ_D	Diffusion time scale	s
ϕ	Porosity	—
ϕ_0	Porosity at $z = 0$	—
ϕ_∞	Porosity at infinite depth	—
ϕ_∞^{calc}	Porosity of pure calcite layer	—
ϕ_∞^{clay}	Porosity of pure clay layer	—
ψ	$(\phi_\infty^{calc} - \phi_\infty^{clay})/(1 - \phi_\infty^{calc})$	—
Ω	$CaCO_3$ saturation	—

$$\phi_\infty = \frac{\phi_\infty^{clay} + f_c\,\psi}{1 + f_c\,\psi} \qquad (2)$$

where $\psi = (\phi_\infty^{calc} - \phi_\infty^{clay})/(1 - \phi_\infty^{calc})$ and ϕ_∞^{clay} and ϕ_∞^{calc} are the porosities of a pure clay and calcite layer, respectively. In the sediment model, the asymptotic porosity, ϕ_∞, significantly below the sediment–water interface is based on

$\phi_\infty^{clay} = 0.82$, $\phi_\infty^{calc} = 0.61$ and f_c-dependent porosity given by Eq. (2).

Observations also show that porosity increases towards the sediment–water interface. In the model, ϕ increases according to:

$$\phi = \phi_\infty + (\phi_0 - \phi_\infty)\exp(-z/z_\phi)$$

where ϕ_0 is the porosity at $z = 0$ and z_ϕ is the porosity attenuation depth. Literature values of ϕ_0 and z_ϕ relevant to the present study are $\phi_0 = 0.8–1.0$ and $z_\phi = 0.25–5$ cm (Martin and Sayles, 1996; Reimers et al., 1996; Archer et al., 1998; Luff and Wallmann, 2003). The default values used in the model are $\phi_0 = 0.9$ and $z_\phi = 2.5$ cm. For the simulations in the Santa Barbara Basin and at Hydrate Ridge, z_ϕ was set to 3.6 and 4.5 cm, respectively (Meysman et al., 2003; Luff and Wallmann, 2003). Finally, given these values and the carbonate fraction, ϕ_∞ and thus ϕ can be determined.
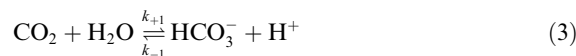
The sediment diffusion coefficients are based on those in seawater (Table 2), corrected for tortuosity:

$$D_{sed} = D_{sw}\phi^{1.7}$$

(Martin and Sayles, 1996). The dependence of diffusion coefficients on temperature was taken into account using previously published relationships (Li and Gregory, 1974; Mackin, 1986; Jähne et al., 1987; Boudreau and Canfield, 1993; Boudreau, 1997).

2.2. Kinetics of acid dissociation

In order to evaluate the assumptions of local chemical equilibrium models vs. a kinetic formulation (see Section 3), the kinetics of the following reactions are included in the current model:

$$CO_2 + H_2O \underset{k_{-1}}{\overset{k_{+1}}{\rightleftharpoons}} HCO_3^- + H^+ \qquad (3)$$

$$CO_2 + OH^- \underset{k_{-4}}{\overset{k_{+4}}{\rightleftharpoons}} HCO_3^- \qquad (4)$$

$$CO_3^{2-} + H^+ \underset{k_{-5}}{\overset{k_{+5}}{\rightleftharpoons}} HCO_3^- \qquad (5)$$

$$H_2O \underset{k_{-6}}{\overset{k_{+6}}{\rightleftharpoons}} H^+ + OH^- \qquad (6)$$

$$B(OH)_3 + OH^- \underset{k_{-7}}{\overset{k_{+7}}{\rightleftharpoons}} B(OH)_4^- \qquad (7)$$

$$HS^- + H^+ \underset{k_{-9}}{\overset{k_{+9}}{\rightleftharpoons}} H_2S \qquad (8)$$

where k's are reaction constants (Zeebe and Wolf-Gladrow, 2001; Zeebe et al., 2001). The time scales of reactions (3) and (7) are of importance in the following because they are much slower than the remaining proton transfer reactions, which are extremely fast (diffusion-controlled). Reactions (3)–(8) lead to kinetic reaction terms, which are included in the respective R_i expressions in Eq. (1). For details, see Zeebe et al. (1999a,b, 2001) and page 291 in Zeebe and Wolf-Gladrow (2001).

The effect of pressure on equilibrium constants was taken into account using published correction coefficients (www.soest.hawaii.edu/oceanography/faculty/zeebe.html; follow book-link). The ratios of kinetic constants for the

Table 2
Diffusion coefficients in seawater[a]

Molecule	No.	$D \times 10^9$ (m² s⁻¹)	Ref.
CO_2	1	1.79	b
HCO_3^-	2	1.10	c
CO_3^{2-}	3	0.89	c
H^+	4	8.68	c
OH^-	5	4.91	c
$B(OH)_3$	6	1.11	d
$B(OH)_4^-$	7	0.97	e
O_2	8	2.17	f
Ca^{2+}	9	0.74	c
$^{13}CO_2$	10	1.79	g
$H^{13}CO_3^-$	11	1.10	c
$^{13}CO_3^{2-}$	12	0.89	c
CH_4	13	1.73	b
SO_4^{2-}	14	1.07	f
H_2S	15	1.87	f
HS^-	16	1.72	f

[a] Values shown (at 25 °C) and temperature dependence applied in the model are based on the references as indicated.
[b] Jähne et al. (1987).
[c] Li and Gregory (1974).
[d] Mackin (1986).
[e] Boudreau and Canfield (1993).
[f] Boudreau (1997).
[g] O'Leary (1984) $D_{^{12}CO_2}/D_{^{13}CO_2} = 1.0007$.

forward and backward reactions were adjusted to be consistent with the equilibrium constants at depth. In the present paper, total dissolved inorganic carbon (TCO_2) and total alkalinity (TA) signify:

$$TCO_2 = [CO_2] + [HCO_3^-] + [CO_3^{2-}],$$
$$TA = [HCO_3^-] + 2[CO_3^{2-}] + [OH^-]$$
$$- [H^+] + [B(OH)_4^-] + [HS^-].$$

2.3. CaCO₃ dissolution and precipitation

Dissolution and precipitation of $CaCO_3$:

$$CaCO_3 \rightarrow Ca^{2+} + CO_3^{2-} \tag{9}$$
$$Ca^{2+} + CO_3^{2-} \rightarrow CaCO_3 \tag{10}$$

lead to source and sink terms for Ca^{2+} and CO_3^{2-} in the model. The calcite dissolution term, R_d, reads (see Table 1 for units):

$$R_d = k_d\, f_c\, (1 - \phi)\, \rho\, (1 - \Omega)^n / a \tag{11}$$

where k_d is the dissolution rate constant, f_c is the solid dry weight fraction of $CaCO_3$, ρ is the solid density, $\Omega = ([CO_3^{2-}][Ca^{2+}]/K_{sp}^*)$, K_{sp}^* is the stoichiometric solubility product of calcite, n is the reaction order, and $a = 100/10^3$ kg mol⁻¹ converts mol C to kg $CaCO_3$. The precipitation of $CaCO_3$ was included in some model experiments (Section 6.2). The precipitation term, R_p, reads:

$$R_p = k_p\, (\Omega - 1)^{n_p} \tag{12}$$

where k_p is the precipitation rate constant and n_p is the reaction order. R_d and R_p are zero above the sediment–water interface ($z < 0$) and for $\Omega > 1$ and $\Omega < 1$, respectively. Due to the inhibiting effect of various seawater ions

on $CaCO_3$ growth, the onset of inorganic precipitation usually requires Ω to be much greater than unity (e.g. Morse and Mackenzie, 1990; Zeebe and Sanyal, 2002). In the model, this behavior was taken into account by linearly decreasing k_p to zero for $3 > \Omega > 1$ (this approach avoided numerical instabilities).

2.4. Stable carbon isotopes

Separate transport-reaction equations (cf. Eq. (1)) for total $C = {}^{12}C + {}^{13}C$ and for ^{13}C for each of the dissolved carbon species CO_2, HCO_3^-, and CO_3^{2-} were solved in the model. Note that solving equations for C and ^{13}C vs. ^{12}C and ^{13}C is equivalent, if done properly (Zeebe et al., 1999a). Fractionation of stable carbon isotopes during CO_2 diffusion was included using:

$$\frac{D_{^{12}CO_2}}{D_{^{13}CO_2}} = 1.0007$$

(O'Leary, 1984). For HCO_3^- and CO_3^{2-}, the diffusion coefficients of the ^{13}C and ^{12}C species were assumed equal. These ions are surrounded by a significant number of water molecules of hydration which contribute to the effective size of the molecule. In comparison to that, the effect of ^{13}C substitution on the diffusion coefficient of the hydrated molecule is likely to be small. Equilibrium isotope fractionation factors were taken from Zhang et al. (1995). Kinetic fractionation factors and rate constants were implemented following procedures described in detail before (Zeebe et al., 1999a,b; Zeebe and Wolf-Gladrow, 2001).

2.5. Organic carbon respiration

The remineralization of organic carbon, which may schematically be written as:

$$CH_2O + O_2 \rightarrow CO_2 + H_2O \tag{13}$$
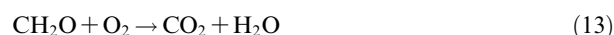
is included in the respective R_i expressions of the solute equations for CO_2, $^{13}CO_2$, and O_2 as an exponential source/sink term:

$$R_{C_{org}}(z) = R_{C_{org}}^0 \exp(-z/z_g)$$

where $R_{C_{org}}^0 = R_{C_{org}}(z = 0)$ is determined from the prescribed depth-integrated total oxidation flux per unit area $F_{C_{org}}$ (in µmol cm⁻² y⁻¹):
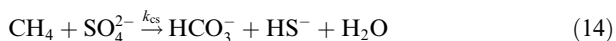
$$F_{C_{org}} = \int_0^l R_{C_{org}}^0 \exp(-z/z_g)\mathrm{d}z$$

where l is the depth of the lower boundary. It follows:

$$R_{C_{org}}^0 = F_{C_{org}}[1 - \exp(-l/z_g)]^{-1}\, z_g^{-1}.$$

The e-folding depth of remineralization in the sediment, z_g, varies depending on the numerical experiment. The $\delta^{13}C$ of respired carbon was set at −22‰.

2.6. Anaerobic oxidation of methane

The model also includes anaerobic oxidation of methane (AOM):

$$CH_4 + SO_4^{2-} \overset{k_{cs}}{\rightarrow} HCO_3^- + HS^- + H_2O \qquad (14)$$

with a kinetic rate expression for CH_4, for example, of:

$$R_{CH_4} = -k_{cs}[CH_4][SO_4^{2-}].$$

Note that the 'rate constant' k_{cs} is expected to be highly variable in space and time because it depends on various environmental parameters, including microbial activity. k_{cs} was tuned to produce agreement between model results and observations (see Section 6.2). I tested a constant and an exponentially decreasing relationship between k_{cs} and depth. The latter approach is based on observed aggregate distributions of archaea/sulfate reducing bacteria in sediments (Boetius et al., 2000). For $k_{cs} = $ const., a value of $1.6 \times 10^4 \, dm^3 \, mol^{-1} \, y^{-1}$ produced reasonable agreement with observations. This value compares well to the order of magnitude of $10^4 \, dm^3 \, mol^{-1} \, y^{-1}$ earlier inferred for this rate constant (Iversen and Jørgensen, 1985; Van Cappellen and Wang, 1996). However, in the model an exponential relationship with attenuation depth of 1 cm was used, which produced better agreement with the data (Section 6.2). The rate constant at $z = 0$ was set at $k_{cs}^{\,0} = 5.4 \times 10^4 \, dm^3 \, mol^{-1} \, y^{-1}$, which yields an average value of $1.8 \times 10^4 \, dm^3 \, mol^{-1} \, y^{-1}$ in the upper 3 cm of sediment.

Note that reaction (14) increases TA and TCO$_2$ in a ratio 2:1. This follows from the explicitly conservative definition of TA in which only the drop in SO_4^{2-} (+2 units of TA) and rise in HCO_3^{2-} (+1 unit of TCO$_2$) need to be considered (Zeebe and Wolf-Gladrow, 2001; Wolf-Gladrow et al., in press). As a result, AOM increases the CaCO$_3$ saturation state and promotes CaCO$_3$ precipitation (Section 6.2, cf. Suess et al., 1999; Han et al., 2004). On the contrary, aerobic methane oxidation $(CH_4 + 2O_2 \rightarrow CO_2 + 2H_2O)$ promotes CaCO$_3$ dissolution.

3. KINETIC VS. LOCAL EQUILIBRIUM MODELS

It is usually assumed that porewater reactions are in local equilibrium because the speed of chemical reactions is much faster than diffusion (e.g. Boudreau, 1987; Archer, 1991;

Martin and Sayles, 1996). This leads to a significant simplification of the equations. Indeed, the time scale of the slowest reaction (CO$_2$ hydration/dehydration) is of the order of minutes or less (e.g. Zeebe et al., 1999b) and thus much smaller than the typical diffusion time scale throughout the model domain, $\tau_D = l^2/D \simeq (0.1 \, m)^2/1 \times 10^{-9} \, m^2/s = 1 \times 10^7 \, s$, or about 4 months. However, this estimate does not consider several other critical issues. The following questions will be addressed below: (1) Is the characteristic time scale of CO$_2$ hydration/dehydration also much smaller than that of dissolution? (2) Given the spatial gradients in $[CO_3^{2-}]$ caused by dissolution, can chemical equilibrium be assumed among all dissolved carbonate species over the relevant length scales? In the following, I will provide contour plots of these critical time and length scales (Figs. 1 and 3). The aim is to assist the reader concerned with the practical application to a specific sediment setting, whether kinetics need to be considered or not.

3.1. Characteristic time scales of CO$_2$ hydration/dehydration and dissolution

If the conversion between HCO_3^- and CO_2 in solution is slower than the release of CO_3^{2-}-ions due to dissolution, then local chemical equilibrium cannot be assumed (note that conversion between CO_3^{2-} and HCO_3^- is practically instantaneous). The characteristic time scale of CO$_2$ hydration/dehydration, τ_{CO_2}, and that of dissolution, τ_d, can be calculated from simplified equations for the time evolution of $[CO_2](t)$ and $[CO_3^{2-}](t)$ (Appendix A). Fig. 1a shows values of τ_{CO_2} based on kinetic rate constants in seawater (Zeebe and Wolf-Gladrow, 2001). At typical deep-sea conditions ($T < 5 \, °C$, pH < 8), τ_{CO_2} is of order 5 min.

Fig. 1b shows values of τ_d as a function of bottom water undersaturation and dissolution rate constant k_d. Undersaturation here is the *in situ* carbonate ion concentration minus the carbonate ion concentration in equilibrium with calcite at *in situ* conditions, $\Delta[CO_3^{2-}] = [CO_3^{2-}] - [CO_3^{2-}]_{sat}$. Only at strong undersaturation of $\Delta[CO_3^{2-}] < -30 \, \mu mol \, kg^{-1}$
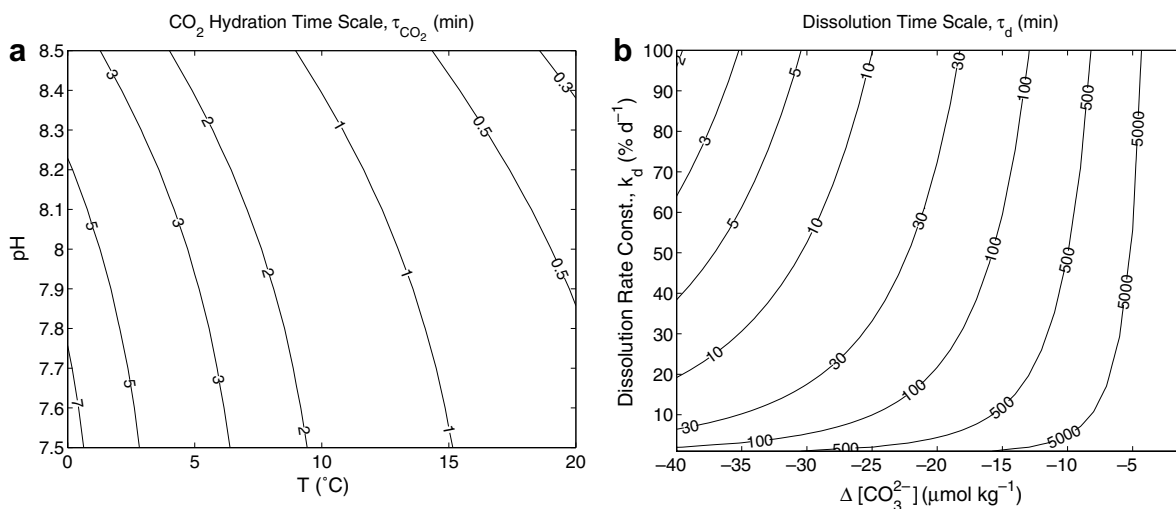

Fig. 1. Characteristic time scale of (a) CO$_2$ hydration, τ_{CO_2}, and (b) dissolution, τ_d, based on analytical solutions (Appendix A). If $\tau_d \lesssim \tau_{CO_2}$, local equilibrium cannot be assumed.

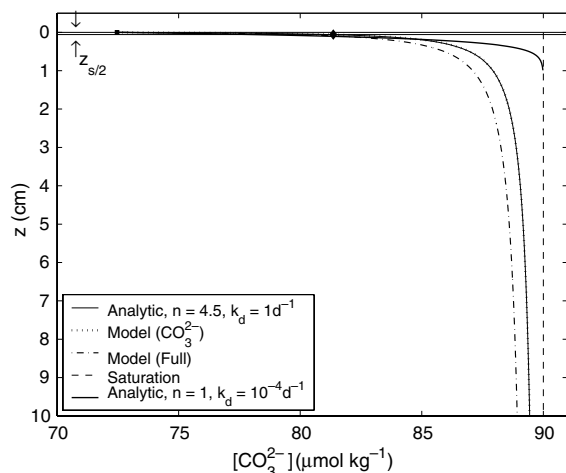Fig. 2. Porewater $[CO_3^{2-}]$ profiles of analytical and numerical solutions (see legend). Note that for $[CO_3^{2-}]$ only ($n = 4.5$, $k_d = 1$ day^{-1}), analytical (thin solid line) and numerical solution (dotted line) are indistinguishable. The full numerical model includes all compounds of the carbonic acid system and Ca^{2+}. The gradient half-width, $z_{s/2}$ (cf. square and diamond), here is a measure of the spatial concentration gradient in $[CO_3^{2-}]$, $l_{\nabla c}$ (see text).

and $k_d > 0.5$ day^{-1} ($n = 4.5$), dissolution becomes as rapid as CO_2 hydration/dehydration at typical deep-sea temperature and pH ($\sim$5 min). Under these conditions ($\tau_d \lesssim \tau_{CO_2}$), local equilibrium can therefore not be assumed. The reverse situation ($\tau_d \gg \tau_{CO_2}$) is a necessary but not sufficient condition for local chemical equilibrium (Section 3.2).

3.2. Length scales of CO_2 reaction/diffusion and gradients in $[CO_3^{2-}]$

Dissolution releases CO_3^{2-}-ions, which leads to spatial gradients in the concentration profile of dissolved CO_3^{2-}.

This, in turn, leads to spatial gradients in $[HCO_3^-]$ and $[CO_2]$ as a result of chemical conversion. The typical length scale of this spatial gradient is denoted here as $l_{\nabla c}$. If $l_{\nabla c}$ becomes sufficiently small, mass transfer by diffusion can become more important than chemical conversion between e.g. HCO_3^- and CO_2, and equilibrium among all dissolved carbonate species can no longer be assumed over this length scale. A quantity used in this context is the reacto-diffusive length scale, $\lambda = (D/k)^{\frac{1}{2}}$, where D is the diffusion coefficient and k is the reaction constant. In order to evaluate the relative importance of diffusion and reaction (and thus the assumption of local chemical equilibrium), λ and $l_{\nabla c}$ need to be compared. Note that these quantities are independent of each other. While λ is a function of the CO_2 hydration rate constant/diffusion coefficient, $l_{\nabla c}$ is a function of CO_3^{2-} undersaturation and the rate expression for $CaCO_3$ dissolution. The square of their ratio $(l_{\nabla c}/\lambda)^2$ is known as the Damköhler number, $Da = (k \cdot l_{\nabla c}^2/D)$ (Damköhler, 1936).

During calcite dissolution, values of $l_{\nabla c}$ can be calculated from a depth-profile of $[CO_3^{2-}]$. With a few assumptions (Appendix B), Eq. (1) including the dissolution term (Eq. (11)), can be solved analytically, if $[CO_3^{2-}]$ is the only chemical species in the calculation. Fig. 2 shows an example of the analytical solution for $[CO_3^{2-}]$, plus the corresponding numerical solutions including only $[CO_3^{2-}]$ and all compounds, respectively. The full numerical model includes all compounds of the carbonic acid system and Ca^{2+}. Note that for CO_3^{2-} only, analytical and numerical solution are indistinguishable, despite a finite lower boundary in the model ($z = 50$ cm vs. $z \to \infty$), confirming that the numerical algorithm works properly. The bottom water undersaturation in this example is $\Delta[CO_3^{2-}] = -18$ μmol kg^{-1}, $k_d = 1$ day^{-1}, and $n = 4.5$. Fig. 2 reveals that strong gradients (i.e. large $\partial[CO_3^{2-}]/\partial z$) are confined to the top 1 mm of the sediment. In this example, the length over which the undersaturation drops by 50% is $z_{s/2} = 0.6$ mm (cf. square and diamond).
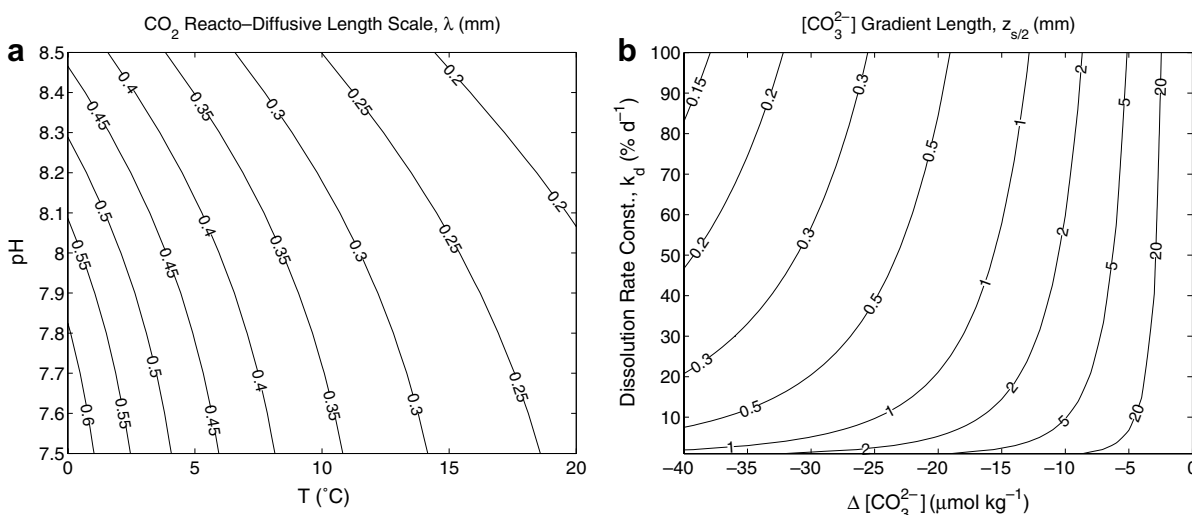

Fig. 3. (a) Reacto-diffusive length scale, λ, of the CO_2 hydration as a function of temperature and pH. (b) Gradient half-width, $z_{s/2}$, based on the analytical solution for $[CO_3^{2-}]$ (Appendix B) as a function of bottom water undersaturation and dissolution rate constant. $[CO_3^{2-}]$ in equilibrium with calcite at *in situ* conditions is $[CO_3^{2-}]_{sat} = 90$ μmol kg^{-1}. For a specific sediment setting at given temperature and pH, comparison between λ and $l_{\nabla c}$ indicates whether kinetics need to be considered or not. For dissolution, $z_{s/2}$ provides a measure of $l_{\nabla c}$.

Fig. 3a shows that at typical deep-sea temperature and pH, λ for the CO_2 hydration reaction, $\lambda = \{D_{CO_2}/(k_{+1} + k_{+4}[OH^-])\}^{\frac{1}{2}}$ is of order 0.5 mm (Zeebe and Wolf-Gladrow, 2001). As a result, $l_{\nabla c}$, which was expressed above in terms of the $[CO_3^{2-}]$-gradient half-width, $z_{s/2}$, is comparable to λ of the CO_2 hydration. This statement holds for a range of commonly used values of n and k_d—the thick solid line in Fig. 2 indicates $n = 1.0$, and $k_d = 1 \times 10^{-4}$ day^{-1} (cf. Archer et al., 1998). Values for $z_{s/2}$ as a function of bottom water undersaturation ($\Delta[CO_3^{2-}]$) and dissolution rate constant k_d, based on the analytical solution at $[CO_3^{2-}]_{sat} = 90$ µmol kg^{-1} are displayed in Fig. 3b. For $\Delta[CO_3^{2-}] < -15$ µmol kg^{-1} and $k_d > 0.5$ day^{-1}, $z_{s/2}$ is smaller than 1 mm and thus of the same order as λ. Note that this range of $\Delta[CO_3^{2-}]$ and k_d (and values of $n = 1.0–4.5$) are relevant to laboratory and field studies as well as local and global models of $CaCO_3$ cycling (e.g. Morse and Mackenzie, 1990; Martin and Sayles, 1996; Archer et al., 1998; Gehlen et al., 1999). For more intense undersaturation or larger values of the dissolution rate constant, the assumption of local chemical equilibrium can therefore not be made. The question arises what are the errors involved in local equilibrium vs. kinetic models? The latter include the full kinetics of the chemical reactions (3)–(8).

3.3. Dissolution and respiration

The model was run with standard values and 10^6-times increased values for the kinetic constants of the boron and CO_2 reactions. (The results with increased constants were found to be very similar to those obtained by calculating CO_2 parameters in local equilibrium from TCO_2 and TA in the standard model.) Fig. 4a shows the difference in the calculated CO_2 concentrations in the two runs (solid and dashed lines) for the above dissolution example ($\Delta[CO_3^{2-}] = -18$ µmol kg^{-1}) and for $\Delta[CO_3^{2-}] = -36$ µmol kg^{-1}. The differences in $[CO_2]$ are small and confined to the upper few millimeter of the sediment (other carbonate species show small effects as well). The calculated

depth-integrated total dissolution is 37.0 (standard) and 39.1 µmol cm^{-2} y^{-1} (fast kinetics). Thus, in this example and considered parameter values, the errors in concentrations and dissolution flux due to the assumption of local equilibrium are small. However, note that fluxes of individual carbonate species (CO_2, CO_3^{2-}, and HCO_3^-) into and out of the sediment ($\propto dc/dz$ at $z = 0$) are significantly different. For example, the dissolved CO_2 flux into the sediment for the equilibrium model is two to three times that of the kinetic model (Fig. 4a, $z = 0$); TCO_2 fluxes are similar.

The effect of organic carbon respiration on CO_2 profiles for the local equilibrium model and the kinetic model are shown in Fig. 4b. In this example, C_{org} respiration is modeled using an exponential decrease with e-folding depths of $z_g = 1$ and 2 mm at a depth-integrated rate of $F_{C_{org}} = 25$ µmol cm^{-2} y^{-1}. Small values of z_g were chosen here because differences between the equilibrium and kinetic model are most pronounced in this case. Yet, the calculated differences in the profiles are small, even at these small values of z_g that are likely restricted to locations with high oxidation rates (cf. Meysman et al., 2003). There was also little difference whether standard or 10^6-times increased rate constants were used for the boron compounds. These reactions are much faster than those for the CO_2 hydration, but slower than diffusion-controlled reactions (Zeebe et al., 2001).

In summary, the assumption of local chemical equilibrium in sediment models appears to be a good approximation in most cases. The kinetics of the CO_2 reactions should be considered when strong gradients exist on length scales below 1 mm (Fig. 3) and if individual fluxes of CO_2, HCO_3^-, and CO_3^{2-} need to be calculated.

4. DIFFUSIVE BOUNDARY LAYER

The transport of dissolved compounds in the water overlying the sediment is usually dominated by eddy diffusion, which is orders of magnitude faster than molecular diffusion. However, close to the sediment–water interface, the mixing decreases and a diffusive boundary layer (DBL)
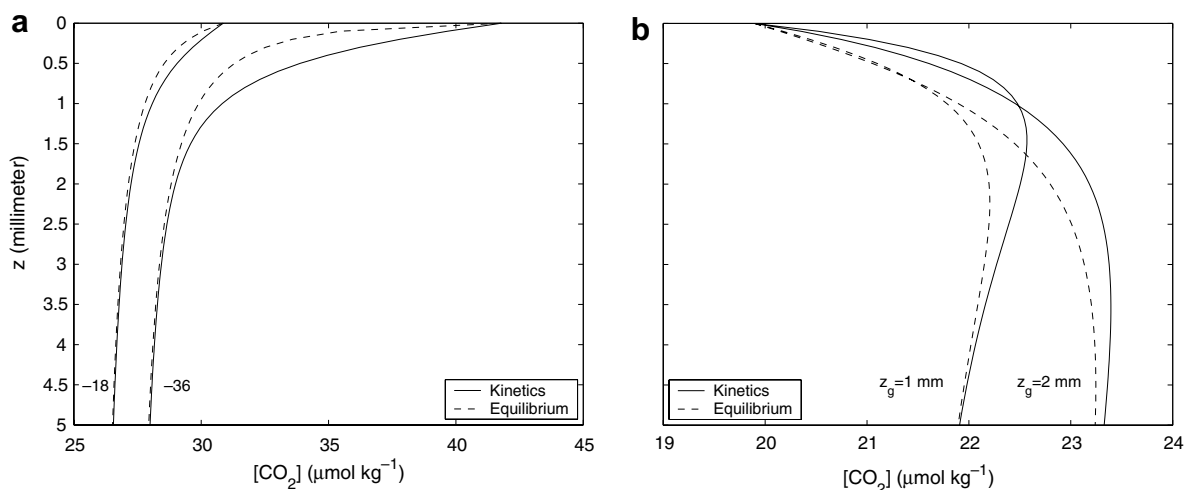

Fig. 4. Differences in calculated CO_2 profiles between equilibrium and kinetic models (see text). (a) Dissolution: undersaturation is -18 (left) and -36 µmol kg^{-1} (right). (b) Organic carbon respiration; z_g is the e-folding depth of remineralization.

develops in which the transport is dominated by molecular diffusion (e.g. Boudreau and Guinasso, 1982; Jørgensen and Revsbech, 1985; Boudreau, 1997). The thickness, δ, of the DBL has been reported to be of order 0.2–1.5 mm in laboratory studies (Jørgensen and Revsbech, 1985), 0.15–2 mm based on chemical fluxes from sea floor experiments (Santschi et al., 1983) and 0.5–3.5 mm based on direct oxygen electrode measurements in deep-sea sediments (Archer et al., 1989).

The diffusive boundary layer is of significance to sediment models because the concentration at the sediment–water interface is commonly assumed to be equal to the bottom water concentration. However, these two concentrations can be very different [for deep-sea sediments, see below and Schink and Guinasso (1977); for a comparative example in a Beggiatoa mat, see Boudreau (1991)]. In the current model, the upper boundary is placed at $z = -\delta$, above the sediment–water interface ($z = 0$) and the transport across the diffusive boundary layer by molecular diffusion is calculated.

4.1. The DBL during dissolution

Fig. 5 shows model concentration profiles for the carbonate species during dissolution, assuming a DBL thickness of 1 mm. The bottom water concentrations are indicated by the upper vertical lines, while the concentrations at the sediment–water interface ($z = 0$, dot-dashed lines) are marked by diamonds. In the example shown, bottom water undersaturation is $\Delta[CO_3^{2-}] = -30$ µmol kg^{-1} which leads to significant concentration differences in the bottom water vs. the sediment–water interface ($z = 0$). For example, the pH at the sediment–water interface is 7.78 compared to 7.71 in the bottom water. The undersaturation at $z = 0$ drops to -19 µmol kg^{-1}, which reduces the calculated CaCO$_3$ dissolution flux by more than a factor of three compared to the case without a DBL. In other words, sediment models which ignore the DBL and assign the bottom water undersaturation to the sediment–water interface may significantly overestimate carbonate dissolution.

The differences in $[CO_3^{2-}]$/pH in the bottom water and at the sediment–water interface as a function of undersaturation are summarized in Fig. 6. Even for moderate undersaturation, the differences are significant. This is illustrated by the gap between model values at $z = 0$ (solid lines with diamonds) vs. a 1:1 correspondence to bottom water (dashed lines). The implications for CO$_2$ system proxies in benthic foraminifera are discussed in Section 7.2.
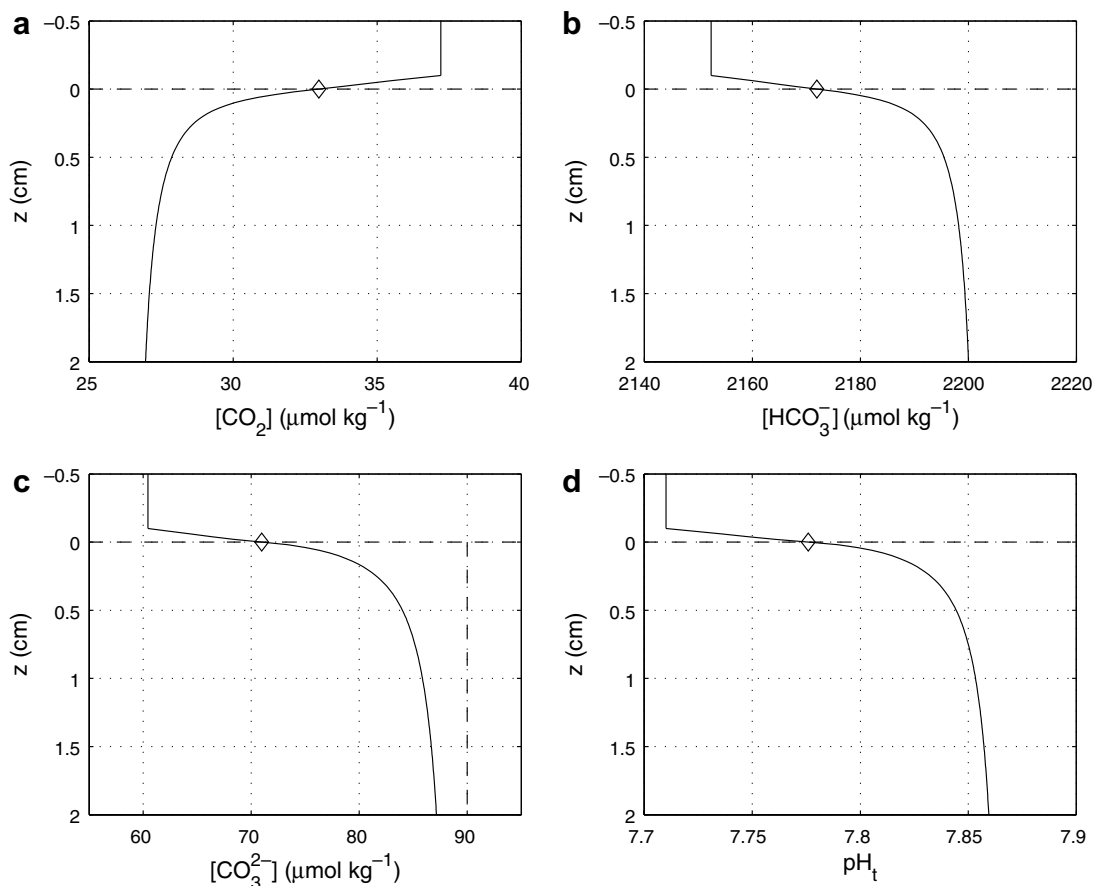

Fig. 5. Diffusive boundary layer during dissolution: porewater profiles of dissolved CO$_2$ compounds. (a) CO$_2$, (b) HCO$_3^-$, (c) CO$_3^{2-}$, and (d) pH (total scale). Bottom water concentrations are indicated by vertical lines, the sediment–water interface is at $z = 0$ (dot-dashed lines).
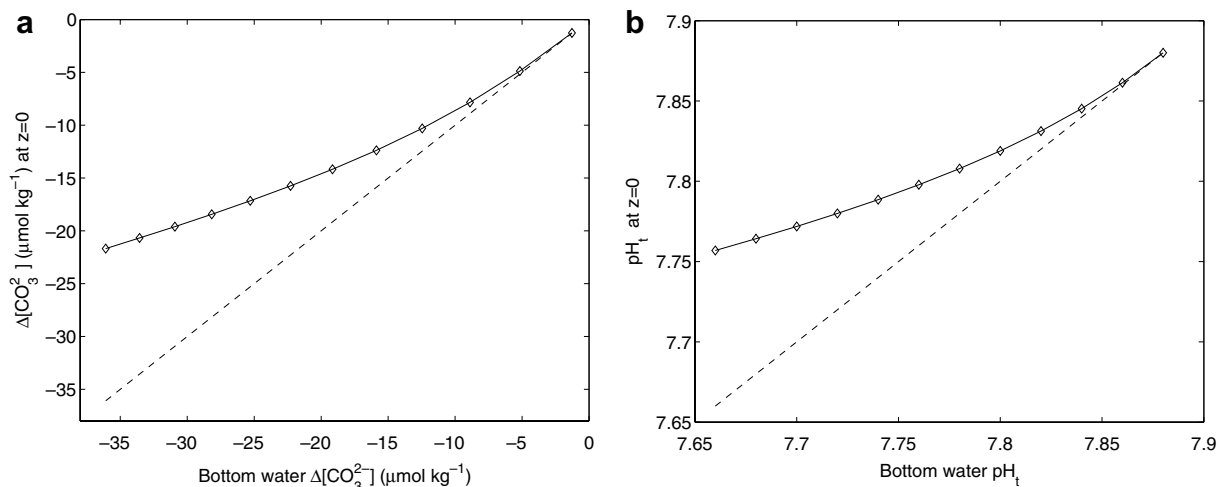
a

b

Fig. 6. Diffusive boundary layer during dissolution: differences between bottom water and sediment–water interface. (a) $\Delta[CO_3^{2-}]$ and (b) pH (total scale). Solid lines with diamonds show model results at $z = 0$. If no differences would exist, a 1:1 correspondence between bottom water and $z = 0$ would be observed (dashed lines).

4.2. The DBL during respiration

Model outcome for C_{org} respiration at a rate of $F_{C_{org}} = 20\ \mu mol\ cm^{-2}\ y^{-1}$ and an e-folding depth of 1 cm are displayed in Fig. 7. While the bottom water is supersaturated with respect to calcite ($[CO_3^{2-}]_{sat} = 85\ \mu mol\ kg^{-1}$), the porewater becomes undersaturated within a few millimeters. This is a result of the CO_2 input, which promotes calcite dissolution in the sediment. In this case, the concentration differences between bottom water and at the sediment–water interface are small. The reason is that here $l_{\nabla c}$ is larger than for the dissolution case (Fig. 5), making properties at $z = 0$ almost equal to those in the bottom water. The same is true for $\delta^{13}C$ of CO_2 and TCO_2 (Figs. 7e and f). However, because of respiration-driven dissolution and input of isotopically light carbon, properties at a sediment depth of 1–2 cm significantly differ from those in the bottom water (Section 5).

5. EFFECTS OF C_{ORG} RESPIRATION ON POREWATER PROFILES

The release of CO_2 during respiration causes strong decreases in porewater $[CO_3^{2-}]$, pH, and $\delta^{13}C_{TCO_2}$ (Figs. 7c, d and f). The isotopically light respired CO_2 ($\delta^{13}C = -22‰$ in the model) is quickly converted into HCO_3^- which makes up more than 95% of porewater TCO_2. As a result, $\delta^{13}C_{TCO_2}$ drops from 0.5‰ in the bottom water to $-1.1‰$ in the porewater at $z = 10$ cm. Thus, porewater saturation, pH, and $\delta^{13}C$ at $z = 2$ cm, for instance, greatly differ from the bottom water conditions. Stable carbon isotopes results presented here are consistent with results of earlier studies (e.g. McCorkle et al., 1985).

Fig. 8 summarizes the difference in $[CO_3^{2-}]$, pH, and $\delta^{13}C_{TCO_2}$ between bottom water and porewater at $z = 2$ cm as a function of the organic carbon respiration rate. The break in slope in $[CO_3^{2-}]$ and pH at $\sim 2\ \mu mol\ cm^{-2}\ y^{-1}$ occurs because the porewater becomes undersaturated at this rate. At higher rates, the dissolution of calcite and addition of CO_3^{2-} and Ca^{2+} to the porewater buffers the acidifying effects of the respired CO_2. The porewater $\delta^{13}C_{TCO_2}$ at the same depth shows a continuous decrease with $F_{C_{org}}$ because the light respired CO_2 dominates the porewater $\delta^{13}C$ profiles. This has consequences for the interpretation of $\delta^{13}C$ and $[CO_3^{2-}]$/pH proxies in benthic foraminifera (Section 7.3).

The respiration rates discussed in this section are typical for deep-sea environments with moderate organic carbon rain rates. Much larger rates are observed, for example, in productive areas on continental shelves (Section 6).

6. ORGANIC CARBON AND METHANE OXIDATION

In the following, the model will be applied to locations of strong oxidation of organic carbon and methane. This includes settings in the Santa Barbara Basin and at Hydrate Ridge at the Cascadia convergent margin.

6.1. Santa Barbara Basin

Kennett et al. (2000) suggested massive methane hydrate dissociation in the Santa Barbara Basin during Quaternary interstadials, which caused strong $\delta^{13}C$ depletions in foraminifera. This hypothesis is controversial and significant clathrate releases during the Younger Dryas-Preboreal Transition, for instance, are unlikely (e.g. Stott et al., 2002; Schaefer et al., 2006). Based on porewater $TCO_2/\delta^{13}C$ measurements, Stott et al. (2002) concluded that methane-derived CO_2 has no discernable effect on porewater $\delta^{13}C$ values in the Santa Barbara and Santa Monica Basins. The lightest porewater $\delta^{13}C$ values of TCO_2 ranged from $-15‰$ to $-17‰$ (Fig. 9) and were assumed to be consistent with a carbon source of $-17‰$. Their result was derived using a simplified model in which TCO_2 and CO_2 were used interchangeably. The current model, in which individual carbonate species and their carbon isotope ratios are
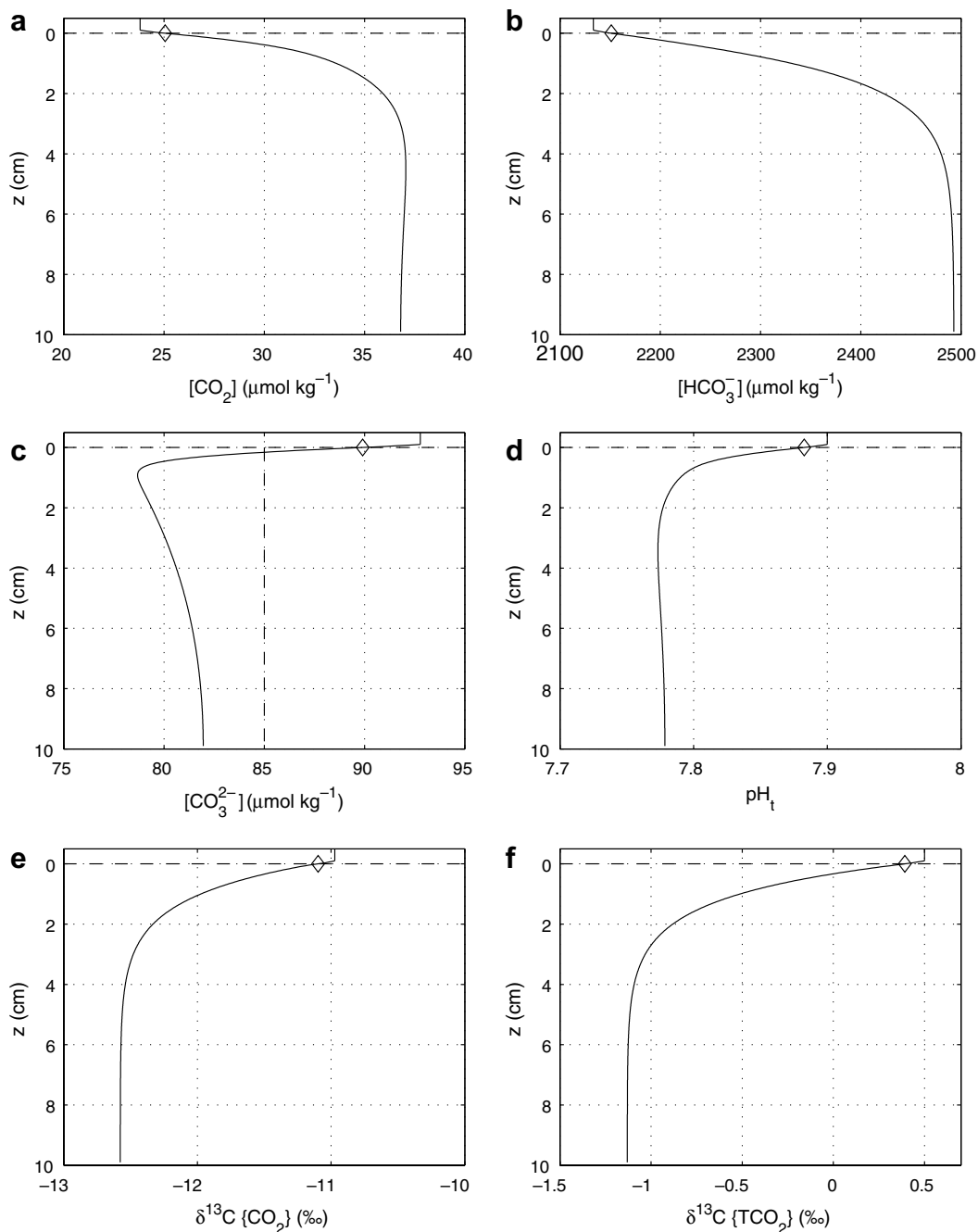
Fig. 7. Diffusive boundary layer during C_{org} respiration: porewater profiles of dissolved compounds. (a) CO_2, (b) HCO_3^-, (c) CO_3^{2-}, (d) pH (total scale), (e) $\delta^{13}C$ of CO_2, and (f) $\delta^{13}C$ of TCO_2. Bottom water concentrations are indicated by upper vertical lines, the sediment–water interface is at $z = 0$ (dot-dashed lines).

treated separately (cf. Zeebe et al., 1999a; Gehlen et al., 1999), yields a different result.

Fig. 9a and b show model results and data for porewater TCO_2 and $\delta^{13}C$ of TCO_2 at the site 'SBBC' (Santa Barbara Basin Center, see Stott et al., 2002). In the model, the amount and location of CO_2 released into the porewater was adjusted to match the observed TCO_2 profile (Fig. 9a). Without further adjustment and a literature value of $\delta^{13}C_{res} = -22\%_0$ for respired CO_2 of organic carbon in

the basin (Schimmelmann and Tegner, 1991), the $\delta^{13}C$ profile of TCO_2 was calculated (Fig. 9b, solid line). This is in excellent agreement with observed porewater $\delta^{13}C_{TCO_2}$ in the upper 10 cm. However, in order to match the data at 40–50 cm depth (oval), a $\delta^{13}C_{res} = -28\%_0$ or lower would be required in the model. This is more than $11\%_0$ lighter than previously assumed. The reason is that in the limit $z \to \infty$, the $\delta^{13}C$ of CO_2 (and not that of TCO_2) approaches that of the respired CO_2 (Fig. 9c). In thermodynamic
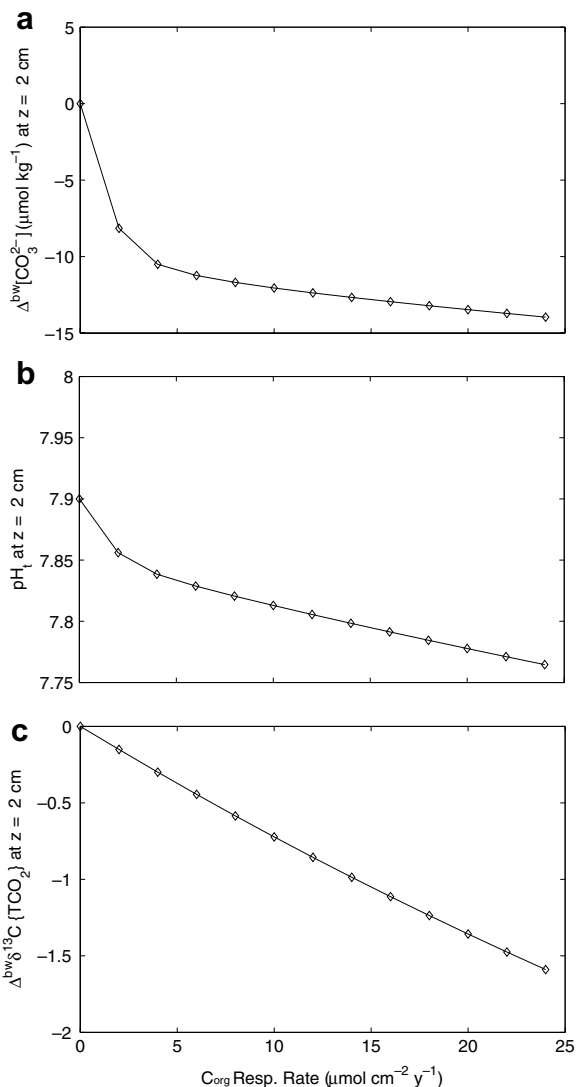
Fig. 8. C_{org} respiration: bottom water vs. porewater properties at $z = 2$ cm. Model results for (a) $\Delta^{bw}[CO_3^{2-}]$, (b) pH (total scale), and (c) $\Delta^{bw}\delta^{13}C$ of TCO_2. Δ^{bw} refers to the difference relative to bottom water. Bottom water pH is 7.9.

Fig. 9. Data (diamonds) and model results (lines) for (a) porewater TCO_2 and (b) $\delta^{13}C$ of TCO_2 at Site 'SBBC' (Santa Barbara Basin Center, see Stott et al., 2002). (c) Model profiles for $\delta^{13}C$ of dissolved CO_2. Solid and dashed lines in (b) and (c) show results assuming a $\delta^{13}C$ of respired CO_2 of -22 and $-28‰$, respectively.

equilibrium at 6 °C, HCO_3^- is 11.2‰ heavier than dissolved CO_2 and at intermediate pH, the majority of TCO_2 is in the form of HCO_3^- (Zeebe and Wolf-Gladrow, 2001). The $\delta^{13}C$ of CO_2 and TCO_2 are only equal at very low pH when the majority of TCO_2 is in the form of CO_2. This is not the case in sediments of this part of the Santa Barbara Basin where carbonate preservation is excellent.

In summary, a CO_2 source of about $-28‰$ is required in order to explain the strongly depleted porewater $\delta^{13}C_{TCO_2}$ values in the Santa Barbara Basin. $\delta^{13}C$ values of bulk organic carbon in sediments of the Santa Barbara and Santa Monica Basins vary roughly between -21 and $-23.5‰$ (Masiello and Druffel, 2003; Cannariato and Stott, 2004). An organic carbon source of $-28‰$ thus appears unlikely and a limited contribution of a more depleted source such as methane-derived CO_2 may be considered. If the ^{13}C depletion is caused by mixing of respired and methane-de-
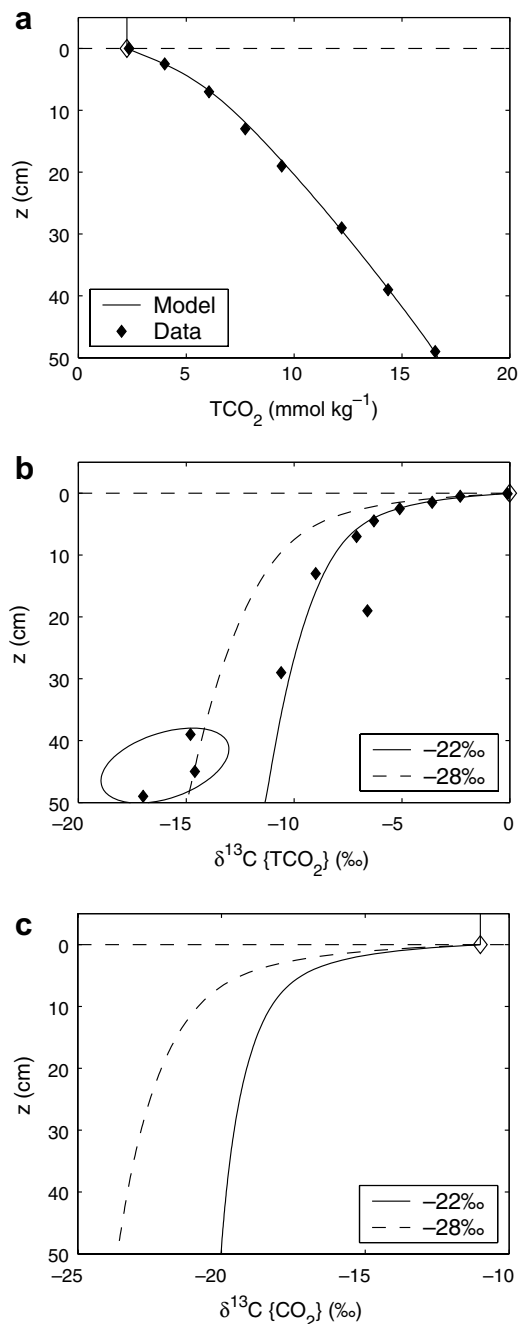
rived CO_2 at $-22‰$ and $-60‰$, respectively, then the methane contribution would be about 10%. However, the advocates of methane clathrates should keep in mind that more strongly depleted $\delta^{13}C_{TCO_2}$ values (three data points) were only found in the lower sediment section at one out of three sites (Stott et al., 2002). The remaining data is well explained by organic carbon respiration.

6.2. Anaerobic oxidation of methane at Hydrate Ridge

At Hydrate Ridge, Cascadia Margin (Suess et al., 1999; Boetius et al., 2000; Luff and Wallmann, 2003; Torres et al., 2004), large rates of anaerobic oxidation of methane (AOM) have been observed, which can lead to extreme ^{13}C depletions in porewater TCO_2 of up to $-50‰$ (Torres et al., 2003). Surprisingly, there appears to be relatively little ^{13}C depletion in the shells of live benthic foraminifera from these vent sites (Torres et al., 2003; Hill et al.,

2004). In order to understand environmental conditions and isotope partitioning during methane discharge, the present model was used to simulate the chemistry and stable carbon isotope ratios in sediment porewaters at Hydrate Ridge.

Fig. 10 shows model results for TCO_2, TA, CH_4, SO_4^{2-}, Ca^{2+}, and TH_2S and data from sediment core SO143/55-2 at the southern summit of Hydrate Ridge, a site characteristic for the occurrence of bacterial mats (Luff and Wallmann, 2003; hereafter LW03). Simulated profiles of
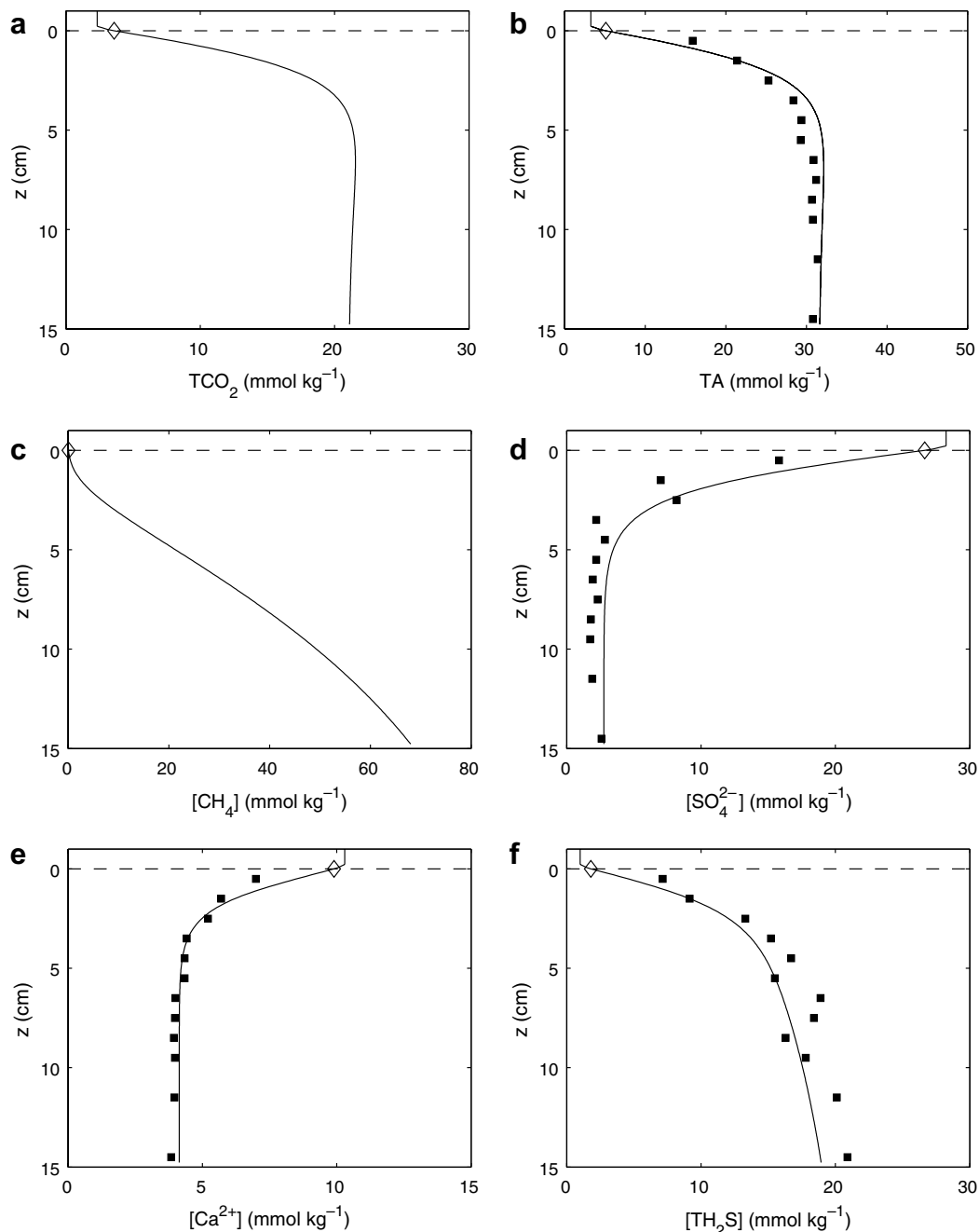

Fig. 10. Model results (lines) and data (squares) for porewater chemistry in core SO143/55-2 at Hydrate Ridge (Luff and Wallmann, 2003). (a) TCO_2, (b) TA, (c) CH_4, (d) SO_4^{2-}, (e) Ca^{2+}, and (f) TH_2S.

compounds for which data is available are in good agreement with observations. The calculated depth-integrated methane oxidation rate at an upward porewater advection of 10 cm y^{-1} is 910 μmol cm^{-2} y^{-1}, close to LW03's model result of 925 μmol cm^{-2} y^{-1}. The current model was set up similar to those of earlier studies (LW03; Aloisi et al., 2004) with a few exceptions. (i) A diffusive boundary layer of 2 mm thickness between bottom water and sediment–water interface was included (cf. Section 4). While its effect on the chemistry is small, it is relevant for stable carbon isotopes (see below). (ii) The rate constant k_{cs} of AOM:

$$CH_4 + SO_4^{2-} \overset{k_{cs}}{\rightarrow} HCO_3^- + HS^- + H_2O \qquad (15)$$
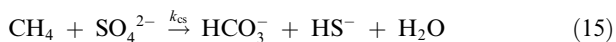
was assumed to decrease exponentially with sediment depth (for values, see Section 2.6). This assumption is based on observed aggregate distributions of archaea/sulfate reducing bacteria in sediments (Boetius et al., 2000). It prevents complete SO_4^{2-} depletion in the lower sediment section and is in better agreement with the observed profile (Fig. 10d). (iii) The order of the rate of $CaCO_3$ precipitation was set to 4.0, in order to match the Ca^{2+} distribution in the upper sediment section (Fig. 10e). Overall, however, LW03's and the current model's results are in good agreement with observations (Fig. 10). This lends confidence to this paper's theoretical description of the porewater chemistry at Hydrate Ridge.

Beyond the porewater chemistry, the current model also allows investigation of stable carbon isotope distributions in porewater. Fig. 11 shows model results for the $\delta^{13}C$ of individual carbonate species and TCO_2 corresponding to Fig. 10. Also shown are porewater $\delta^{13}C_{TCO_2}$ measurements (squares) in core A99-5AD at a bacterial mat site (Torres et al., 2003) in close proximity to core SO143/55-2. (Measured profiles of SO_4^{2-}, Ca^{2+}, and TH_2S are very similar in cores A99-5AD and SO143/55-2). In order to match $\delta^{13}C$ observations, the model requires a methane isotopic
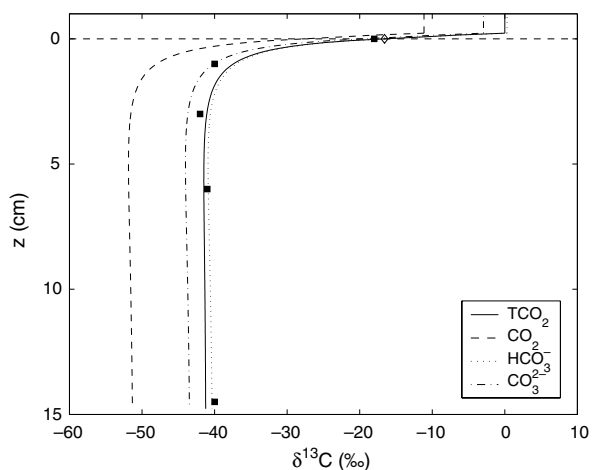

Fig. 12. Model results for porewater $\delta^{13}C_{TCO_2}$ as a function of depth and AOM rates (from 0 to 1044 in μmol cm^{-2} y^{-1}) at $\delta^{13}C_{CH_4} = -60‰$. Diamonds indicate model values at the sediment–water interface.

composition of $\delta^{13}C_{CH_4} = -48‰$. If $\delta^{13}C_{CH_4} = -60‰$ were used, profiles at $z = 15$ cm would be shifted by about 11‰ towards lighter values (see Fig. 12).

A remarkable result of the simulation is that the TCO_2 at the sediment–water interface ($z = 0$, diamond) has a $\delta^{13}C$ value of $-16‰$, compared to $0‰$ in the bottom water. This strong surface depletion is supported by the data at station 5AD, showing values of about $-18‰$ immediately at the sediment surface (Torres et al., 2003). The reason for this is the diffusive boundary layer (Section 4), which causes an offset in chemical concentrations and isotopic compositions between bottom water and sediment–water interface. The effect is likely to be even larger with stronger upward porewater advection. As a corollary, at vent sites with strong methane oxidation and fluid flow, $\delta^{13}C_{TCO_2}$ at the sediment–water interface is expected to be strongly depleted relative to the bottom water (for implications on $\delta^{13}C$ in benthic foraminifera, see Section 7.5).

Note that although methane is converted without fractionation into HCO_3^- in the model (reaction (15)), the asymptotic value of $\delta^{13}C_{HCO_3^-}$ does not approach $-48‰$ at the lower boundary ($z = 15$ cm). Rather, HCO_3^- is about 8‰ heavier. The reason is that diffusive mixing with isotopically heavy carbonate species in the bottom water enriches porewater $\delta^{13}C$ values. Also note that porewater CO_2 approaches a $\delta^{13}C$ value that is lighter than the methane source. As mentioned above, in thermodynamic equilibrium CO_2 is lighter than HCO_3^- (Zeebe and Wolf-Gladrow, 2001). The difference is 11.5‰ at a reported bottom water temperature of 4 °C at Hydrate Ridge (Luff and Wallmann, 2003).

6.2.1. Porewater $\delta^{13}C$ as a function of oxidation Rate

Methane oxidation has a strong effect on porewater $\delta^{13}C$ at all depths, including locations close to or at the sediment–water interface. For example, at an AOM rate of $F_{CH_4} = 910$ μmol cm^{-2} y^{-1} (Fig. 11), $\delta^{13}C_{TCO_2}$ decreases to values below $-35‰$ within the top 1 cm of sediment.

Fig. 11. Model results (solid line) and measurements (squares) for porewater $\delta^{13}C_{TCO_2}$ in core A99-5AD at Hydrate Ridge (Torres et al., 2003). Also shown are $\delta^{13}C$ values of individual carbonate species (see legend). Model $\delta^{13}C_{CH_4}$ is $-48‰$. The diamond indicates model $\delta^{13}C_{TCO_2}$ at the sediment–water interface; note the difference to bottom water (upper vertical solid line).
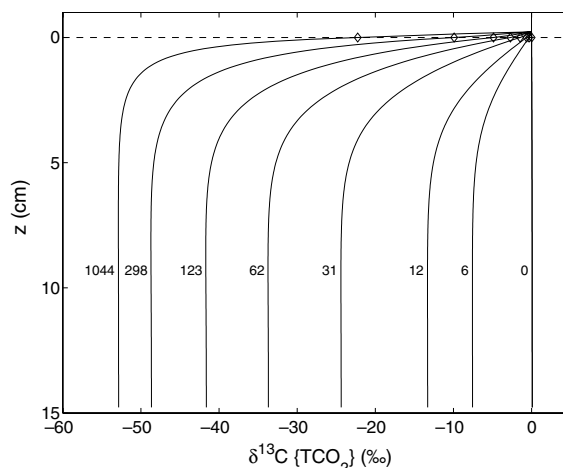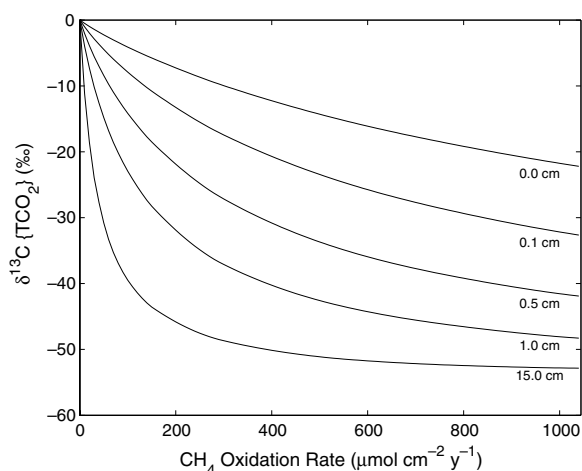
Fig. 13. Model results for porewater $\delta^{13}C_{TCO_2}$ as a function of AOM rate at different sediment depths (from 0 to 15 cm); $\delta^{13}C_{CH_4} = -60‰$.

Fig. 12 shows $\delta^{13}C_{TCO_2}$ profiles at different AOM rates using $\delta^{13}C_{CH_4} = -60‰$. Diamonds indicate $\delta^{13}C_{TCO_2}$ values at the sediment–water interface ($z = 0$). The $\delta^{13}C$ of porewater TCO_2 decreases in a non-linear fashion with F_{CH_4}. At an AOM rate of only $\sim 60\ \mu mol\ cm^{-2}\ y^{-1}$, $\delta^{13}C_{TCO_2}$ values below 4 cm are lighter than $-30‰$, while at rates $>300\ \mu mol\ cm^{-2}\ y^{-1}$, the saturation value of $-53‰$ is quickly approached. A further increase of F_{CH_4} has little effect.

This behavior is illustrated in Fig. 13 which shows $\delta^{13}C_{TCO_2}$ as a function of the oxidation rate at different sediment depths. For example, the graph for $z = 15$ cm drops quickly to strongly depleted values but is flat at high AOM rates. Differences in the response of $\delta^{13}C_{TCO_2}$ to the oxidation rate at different sediment depths are restricted to within and above the anaerobic methane oxidation zone in the top few centimeters of sediment. This zone is relatively narrow because the reaction is limited by $k_{cs}(z)$ below ~ 4 cm (Fig. 10d), while $[CH_4]$ limits the reaction above this depth (Fig. 10c). As a result, strong gradients in TCO_2 and its carbon isotopes only occur close to the sediment surface. In the lower sediment section, profiles are nearly constant. In other words, differences between e.g. $z = 1$ cm and 15 cm are small (Fig. 13). Note also that even at $z = 0$ cm, depletions by more than 10–20‰ can occur relative to the bottom water because of the effect of the diffusive boundary layer (see above).

7. SUMMARY AND IMPLICATIONS

In the following, the different results of the present study are summarized and their implications for numerical sediment modeling, carbon and methane cycling, and paleoproxies in benthic foraminifera are discussed.

7.1. Numerical sediment models: kinetics vs. equilibrium

I have demonstrated that under specific circumstances, the assumption of local chemical equilibrium cannot be made in numerical sediment models. However, the errors introduced by local equilibrium vs. kinetic models are likely small in most cases (Section 3). Errors may be significant when strong gradients exist on length scales below 1 mm and when individual fluxes of CO_2, HCO_3^-, and CO_3^{2-} need to be calculated. In this case, the kinetics of the CO_2 reactions should be considered.

7.2. Diffusive boundary layer

Inclusion of a DBL in numerical sediment models seems critical. Observations in the deep-sea show a DBL thickness of about 1 mm (Archer et al., 1989). Numerical models that ignore a DBL of this thickness, may overestimate $CaCO_3$ dissolution by a factor of three or so at strong undersaturation (Section 4). It is noted that Schink and Guinasso (1977) already mentioned that the effect of a DBL on carbonate dissolution deserves more attention in sediment models. Simulation of porewater $\delta^{13}C_{TCO_2}$ without a DBL also leads to incorrect results. The effects of the DBL become particularly important if, for example, strongly enriched or depleted carbon sources are involved (Fig. 11). Models lacking a DBL assume the bottom water value at the sediment–water interface. However, as the current model and observations show, at methane vents $\delta^{13}C_{TCO_2}$ at $z = 0$ can be depleted by more than 10‰ relative to the bottom water (Fig. 11).

The presence of a DBL during dissolution also has implications for CO_2 system proxies in benthic foraminifera, because $[CO_3^{2-}]/pH$ at the sediment–water interface and in the bottom water are different (Fig. 6). During dissolution, benthic foraminifera living at the sediment–water interface would record a smaller $\Delta[CO_3^{2-}]$ and higher pH than actually exist in the bottom water. This, and other complications associated with dissolution can be avoided by focusing on sediment cores located above the lysocline, which is, in fact, the case for many paleoceanographic studies. However, caution is advised if CO_2 system proxies in benthic foraminifera are applied during transient dissolution events (for example, during the Paleocene-Eocene Thermal Maximum). Even if direct dissolution effects on elemental and isotopic ratios in the shells of foraminifera are minimal, the existence of the DBL prevents a precise recording of CO_3^{2-} and pH during strong undersaturation. Paleorecords would tend to underestimate both $\Delta[CO_3^{2-}]$ and the drop in pH (Fig. 6).

7.3. Organic carbon respiration

Paleorecords in benthic foraminifera can also be influenced by dissolution even if the core was located above the lysocline. For example, respiration-driven dissolution can lead to significant differences between properties in the bottom water and in the top few cm of sediment (Fig. 8). The calculated differences in $[CO_3^{2-}]$, pH, and $\delta^{13}C_{TCO_2}$ at 2 cm are about $-10\ \mu mol\ kg^{-1}$, -0.1 pH units, and $-1‰$ at a moderate rate of $F_{C_{org}} \sim 12\ \mu mol\ cm^{-2}\ y^{-1}$. Such differences, even if only partly reflected in the shells of benthic foraminifera, can be significant for paleoceanographic reconstructions (e.g. McCorkle et al., 1985; Sanyal et al., 1995; Boyle, 1997; Hönisch et al., 2006; Yu and Elderfield, 2006).

7.4. Santa Barbara Basin

Application of the model to sediments in the Santa Barbara Basin showed that porewater TCO_2 and $\delta^{13}C_{TCO_2}$ can be satisfactorily simulated (Fig. 9). I have demonstrated that in order to infer the isotopic composition of the source that causes the porewater ^{13}C depletions, separate ^{13}C equations for individual carbonate species need to be solved (cf. Zeebe et al., 1999a; Gehlen et al., 1999). The reason is that in thermodynamic equilibrium at 6 °C, for instance, HCO_3^- is 11.2‰ heavier than dissolved CO_2. As a result, a CO_2 source of about −28‰ is required to explain the most depleted porewater $\delta^{13}C_{TCO_2}$ values in the Santa Barbara Basin. A methane contribution of the order of 10% cannot be ruled out. However, with regard to the significance of methane fluxes in the Santa Barbara/Santa Monica Basins (cf. Kennett et al., 2000), it is noted that more strongly depleted $\delta^{13}C_{TCO_2}$ values were observed only for three data points from the lower sediment section at one out of three sites (Stott et al., 2002). The remaining data are consistent with organic carbon respiration.

7.5. Hydrate Ridge

Model results for the chemistry and stable carbon isotope ratios in porewaters at Hydrate Ridge are in good agreement with data (Figs. 10 and 11). An important result of this study is that even at moderate anaerobic methane oxidation rates ($F_{CH_4} \sim 50$ μmol cm^{-2} y^{-1}), porewater $\delta^{13}C_{TCO_2}$ at $z = 1$ cm is depleted by more than 15‰ relative to bottom water (Fig. 13). However, shells of live benthic foraminifera from these sites do generally not show ^{13}C depletions of this magnitude, although their $\delta^{13}C$ appears to be more depleted at methane vents than at non-venting sites. The $\delta^{13}C$ of live (stained) foraminifera at Hydrate Ridge ranged from 0‰ to −4‰ (Torres et al., 2003) and averaged about −2.5‰ in 84 specimen analyzed (Hill et al., 2004). To the best of my knowledge, the lightest values so far reported are −9.0‰ and −12.6‰ in two stained *Uvigerina peregrina* specimen (Hill et al., 2004). [Note that the 'D = dead'-labels for these specimen in Table 3 of Hill et al. (2004) are misprints. The correct label should be 'L = live'; Tessa Hill, personal communication 2007.] Regarding the method used to identify live and dead specimen, a note of caution is in order. The conventional staining technique applied by Torres et al. (2003) and Hill et al. (2004) which uses Rose Bengal is indicative of the presence of cytoplasm but not necessarily of a living organism. A recent study has shown that this technique may overestimate the number of living specimen by more than 50% (Bernhard et al., 2006).

In contrast to foraminifera, inorganic carbonates on the northern Hydrate Ridge have $\delta^{13}C$ values of −51‰ (Torres et al., 2003). Strongly depleted values have also been found in authigenic carbonates formed at other vent sites, for example on the Costa Rica margin (Han et al., 2004). Dead benthic and planktonic foraminifera from Hydrate Ridge also exhibit more depleted values of up to −9.8‰ (Torres et al., 2003) and −21.6‰ (Hill et al., 2004). Yet, this is not the case for living benthic foraminifera at Hydrate Ridge or at a methane seep in Monterey Bay, for example

(Rathburn et al., 2003; Martin et al., 2004). ^{13}C depletions of −7.5‰ relative to bottom water in stained specimen were reported for *Cassidulina neoteretis* at a cold seep off Norway (Mackensen et al., 2006). Although this value is lighter than reported for many other living specimen at vent sites, it is still significantly heavier than the average porewater $\delta^{13}C_{TCO_2}$ of −18.7‰ in the top 3 cm at this site (Lein et al., 1999).

Understanding this phenomenon is important for a variety of reasons. For example, if the interstadial ^{13}C depletions in fossil foraminifera as reported by Kennett et al. (2000) were recorded by live benthic and planktic foraminifera, then the argument can be made that the entire water column was strongly depleted due to a potentially massive release of methane carbon. However, if the observed depletions are due to secondary overprints within the sediment after the shells were deposited, then methane hydrate dissociation may have had effects on the local sediment geochemistry, but not on the water column at the basin-scale.

The current model shows that porewater $\delta^{13}C_{TCO_2}$ values of −15 to −50‰ can be easily achieved below a sediment depth of 1 cm at realistic AOM rates (Fig. 13). However, living benthic foraminifera at today's methane vents apparently lack such depletions. This suggests that foraminifera at vent sites either calcify at very shallow sediment depths or during times when oxidation rates are much lower than $\sim$50 μmol cm^{-2} y^{-1}. Until this issue is resolved, the hypothesis that strong ^{13}C depletions due to methane discharge were recorded by live specimen in the past, remains to be tested.

7.6. Prospects

Based on the results and implications summarized above, I conclude that the model presented here is a useful theoretical tool to advance our understanding of sediment geochemistry and paleo-proxy validation in benthic foraminifera. Regarding stand-alone sediment models as well as those embedded in general circulation models, I suggest that diffusive boundary layer effects on calculated $CaCO_3$ dissolution rates should be considered in future work. It is also desirable that experimental and theoretical proxy validation in benthic foraminifera will follow a path similar to that recently taken for planktonic foraminifera. I hope that the insights gained from the present study will contribute to this.

APPENDIX A. CHARACTERISTIC TIME SCALES

The characteristic time scale (*e*-folding time) of the CO_2 hydration can be calculated from:

$$\frac{d[CO_2]}{dt} = -k_{CO_2}[CO_2]$$

where $k_{CO_2} = k_{+1} + k_{+4}[OH^-]$ (Zeebe and Wolf-Gladrow, 2001). The solution is of the form $e^{-k_{CO_2} \cdot t}$ and the characteristic time scale is simply $\tau_{CO_2} = k_{CO_2}^{-1}$ (Fig. 1a).

The characteristic time scale of dissolution can be calculated from Eq. (1), considering only $[CO_3^{2-}]$ ($=c$ here) and the dissolution term (Eq. (11)):

$$\frac{dc}{dt} = \beta(1 - c/c_s)^n$$

where $\beta = k_d f_c (1 - \phi) \rho/\phi/a$ and c_s is the saturation concentration. Using $s = 1 - c/c_s$, it follows:

$$\frac{ds}{dt} = -\frac{\beta}{c_s} s^n$$

and separation of variables gives:

$$\frac{ds}{s^n} = -\frac{\beta}{c_s} dt.$$

Integration from s_0 to s and 0 to t yields:

$$\frac{s^{(1-n)} - s_0^{(1-n)}}{1 - n} = -\frac{\beta}{c_s} t$$

and thus:

$$s = \left[s_0^{(1-n)} - \frac{\beta(1-n)}{c_s} t \right]^{\frac{1}{1-n}}.$$

The dissolution time scale, τ_d, after which $s(t)$ has decreased to $1/e$ of its initial value can be calculated from:

$$\frac{(s_0/e)^{(1-n)} - s_0^{(1-n)}}{1 - n} = -\frac{\beta}{c_s} \tau_d$$

which yields:

$$\tau_d = s_0^{(1-n)} [e^{(n-1)} - 1] \frac{c_s}{\beta (n - 1)}.$$

Values of τ_d are shown in Fig. 1b.

APPENDIX B. DISSOLUTION: ANALYTICAL SOLUTION

The DEQ for $[CO_3^{2-}]$ ($=c$ here) reads:

$$0 = \frac{\partial(\phi c)}{\partial t}$$
$$= \frac{\partial}{\partial z}\left(\phi D_i \frac{\partial c}{\partial z}\right) - \frac{\partial(\phi w c)}{\partial z} + k_d f_c(1 - \phi)\rho(1 - \Omega)^n/a + \ldots$$

and may be simplified to include diffusion and dissolution only (Boudreau and Guinasso, 1982; Keir, 1982). Assuming ϕ, D, and $[Ca^{2+}]$ constant, and $w = 0$:

$$0 = \phi \frac{\partial c}{\partial t} = \phi D \frac{\partial^2 c}{\partial z^2} + \zeta f_c (1 - c/c_s)^n$$

where $\zeta = k_d (1 - \phi) \rho/a$ and c_s is the saturation concentration. Or:

$$0 = \frac{\partial^2 c}{\partial z^2} + \frac{\zeta f_c}{\phi D}(1 - c/c_s)^n.$$

Substitute $s = 1 - c/c_s$ and note that $\frac{ds}{dz} = -\frac{1}{c_s}\frac{dc}{dz}$ from which follows:

$$0 = \frac{d^2 s}{dz^2} - \gamma s^n$$

where $\gamma = \zeta f_c/c_s/\phi/D$. To obtain the first integral, let $y = ds/dz$, then we can write:

$$\frac{d^2 s}{dz^2} = \frac{dy}{dz} = \frac{dy}{ds}\frac{ds}{dz} = y\frac{dy}{ds}$$

and hence:

$$0 = y\frac{dy}{ds} - \gamma s^n.$$

Separation of variables and integration gives:

$$\frac{1}{2}y^2 = \frac{\gamma}{n+1}s^{n+1} + A.$$

In the limit $z \to \infty$, $y = ds/dz \to 0$ and $s \to 0$ (zero flux at lower boundary and porewater saturation, i.e. $c = c_s$). Thus $A = 0$. Taking the negative root, we have:

$$y = \frac{ds}{dz} = -\left[\frac{2\gamma}{n+1}s^{n+1}\right]^{1/2} \tag{B1}$$

From this, the dissolution flux at $z = 0$ can be determined:

$$F_{diss} = \phi D\frac{dc}{dz}\bigg|_0 = -\phi D c_s\frac{ds}{dz}\bigg|_0 = \phi D c_s\left[\frac{2\gamma}{n+1}s_0^{n+1}\right]^{1/2}.$$

Eq. (B1) can be integrated to yield s and thus $c = c_s(1 - s)$. Let $g = [2\gamma/(n+1)]^{1/2}$, then

$$g^{-1}s^{-\frac{n+1}{2}}ds = -dz.$$

After integration, the exponent of s will be $-(n+1)/2 + 1 = (-n-1+2)/2 = (1-n)/2 =: m$. Thus integrating from z_0 to z and s_0 to s yields:

$$g^{-1} m^{-1}(s^m - s_0^m) = -(z - z_0)$$

and using $z_0 = 0$,

$$s^m = s_0^m - z m g$$

or:

$$s = \left[s_0^m - z m \left(\frac{2\gamma}{n+1}\right)^{1/2}\right]^{1/m} \tag{B2}$$

where $s = 1 - c/c_s$ and $m = (1 - n)/2$. The depth $z_{s/2}$ at which the saturation s (proportional to carbonate ion concentration, c) drops to 50% is given by:

$$(s_0/2)^m = s_0^m - z_{s/2} m g$$

or

$$z_{s/2} = \frac{s_0^m - (s_0/2)^m}{m g} \tag{B3}$$

REFERENCES

Aloisi G., Wallmann K., Bollwerk S. M., Derkachev A., Bohrmann G., and Suess E. (2004) The effect of dissolved barium on biogeochemical processes at cold seeps. *Geochim. Cosmochim. Acta* **68**(8), 1735–1748.

Archer D. (1991) Modeling the calcite lysocline. *J. Geophys. Res.* **96**, 17037–17050.

Archer D., Kheshgi H., and Maier-Reimer E. (1998) Dynamics of fossil fuel CO_2 neutralization by marine $CaCO_3$. *Global Biogeochem. Cycles* **12**, 259–276.

Archer D., Emerson S., and Smith C. R. (1989) Direct measurement of the diffusive sublayer at the deep sea floor using oxygen microelectrodes. *Nature* **340**, 623–626.

Berner R. A. (1980) *Early Diagenesis: A Theoretical Approach*. Princeton University Press, Princeton, pp. 241.

Bernhard J. M. and Sen Gupta B. K. (1999) Foraminifera of oxygen-depleted environments. In *Modern Foraminifera* (ed. B. K. Sen Gupta). Kluwer Academic, pp. 201–216.

Bernhard J. M., Ostermann D. R., Williams D. S., and Blanks J. K. (2006) Comparison of two methods to identify live benthic foraminifera: a test between Rose Bengal and CellTracker Green with implications for stable isotope paleoreconstructions. *Paleoceanography* **21**, PA4210. doi:10.1029/2006PA001290.

Boetius A., Ravenschlag K., Schubert C. J., Rickert D., Widdel F., Gieseke A., Amann R., Jørgensen B. B., Witte U., and Pfannkuche O. (2000) A marine microbial consortium apparently mediating anaerobic oxidation of methane. *Nature* **407**, 623–626.

Boudreau B. P. (1987) A steady-state diagenetic model for dissolved carbonate species and pH in the porewaters of oxic and suboxic sediments. *Geochim. Cosmochim. Acta* **51**, 1985–1996.

Boudreau B. P. (1991) Modelling the sulfide–oxygen reaction and associated pH gradients in porewaters. *Geochim. Cosmochim. Acta* **55**, 145–159.

Boudreau B. P. (1997) *Diagenetic models and their implementation*. Springer-Verlag, New York, pp. 414.

Boudreau B. P., and Canfield D. E. (1993) A comparison of closed- and open-system models for porewater pH and calcite-saturation state. *Geochim. Cosmochim. Acta* **57**, 317–334.

Boudreau B. P. and Guinasso N. L. (1982) The influence of a diffusive sublayer on accretion, dissolution and diagenesis at the sea floor. In *The Dynamic Environment of the Ocean Floor* (eds. K. A. Fanning and F. T. Manheim). Lexington Books, pp. 115–145.

Boyle E. A. (1997) Characteristics of the deep ocean carbon system during the past 150,000 years: ΣCO_2 distributions, deep water flow patterns, and abrupt climate change. *Proc. Natl. Acad. Sci. USA* **94**, 8300–8307.

Broecker W. S. and Takahashi T. (1997) Neutralization of fossil fuel CO_2 by marine calcium carbonate. In *The Fate of Fossil Fuel CO_2 in the Oceans* (eds. N. R. Anderson and A. Malahoff). Plenum Press, New York, pp. 213–241.

Buffett B., and Archer D. (2004) Global inventory of methane clathrate: sensitivity to changes in the deep ocean. *Earth Planet. Sci. Lett.* **227**, 185–199.

Cannariato K. G., and Stott L. D. (2004) Evidence against clathrate-derived methane release to Santa Barbara Basin surface waters? *Geochem. Geophys. Geosyst.* **5**(5), Q05007. doi:10.1029/2003GC000600.

Curry W. B., and Oppo D. W. (2005) Glacial water mass geometry and the distribution of $\delta^{13}C$ of ΣCO_2 in the western Atlantic Ocean. *Paleoceanography* **20**, PA1017. doi:10.1029/2004PA001021.

Damköhler G. (1936) Einflüsse der Strömung, Diffusion und des Wärmeüberganges auf die Leistung von Reaktionsöfen. *Zeitschr. Elektrochem.* **42**(12), 846–862.

Gehlen M., Mucci A., and Boudreau B. P. (1999) Modelling the distribution of stable carbon isotopes in porewaters of marine sediments. *Geochim. Cosmochim. Acta* **63**(18), 2763–2773.

Gornitz V., and Fung I. (1994) Potential distribution of methane hydrate in the world's oceans. *Glob. Biogeochem. Cycles* **8**, 335–347.

Han X., Suess E., Sahling H., and Wallmann K. (2004). *Fluid venting activity on the Costa Rica marg new results from authigenic carbonates. Int. J. Earth Sci. (Geol. Rundsch.)* **93**, 596–611. doi:10.1007/s00531–004–0402–y.

Herbert T. D., and Mayer L. A. (1991) Long climatic time series from sediment physical property measurements. *J. Sed. Petrol.* **61**(7), 1089–1108.

Hill T. M., Kennett J. P., and Valentine D. L. (2004) Isotopic evidence for the incorporation of methane-derived carbon into foraminifera from modern methane seeps, Hydrate Ridge, Northeast Pacific. *Geochim. Cosmochim. Acta* **68**(22), 4619–4627.

Hintz C. J., Chandler G. T., Bernhard J. M., McCorkle D. C., Havach S. M., Blanks J. K., and Shaw T. J. (2004) A physicochemically constrained seawater culturing system for production of benthic foraminifera. *Limnol. Oceanogr.: Methods* **2**, 160–170.

Hönisch B., Hemming G., and Bickert T. (2006) Paleo-validation of the boron isotope proxy in benthic and planktic foraminifers. *Eos Trans AGU* **87**(36), Ocean Sci. Meet. Suppl., Abstract OS42E–01.

Iversen N., and Jørgensen B. B. (1985) Anaerobic methane oxidation rates at the sulfate-methane transition in marine sediments from Kattegat and Skagerrak (Denmark). *Limnol. Oceanogr.* **30**, 944–955.

Jähne B., Heinz G., and Dietrich W. (1987) Measurement of the diffusion coefficients of sparingly soluble gases in water. *J. Geophys. Res.* **92**, 10767–10776.

Jørgensen B. B., and Revsbech N. P. (1985) Diffusive boundary layers and the oxygen uptake of sediments and detritus. *Limnol. Oceanogr.* **30**(1), 111–122.

Keir R. (1982) Dissolution of calcite in the deep sea: Theoretical predictions for the case of uniform size particles settling into a well-mixed sediment. *Am. J. Sci.* **282**, 193–236.

Kennett J. P., Cannariato K. G., Hendy I. L., and Behl R. J. (2000) Carbon isotopic evidence for methane hydrate instability during Quarternary interstadials. *Science* **288**, 128–133.

Kvenvolden K. A. (1988) Methane hydrates and global climate *Glob. Biogeochem. Cycles* **2**, 221–229.

Lein A., Vogt P., Crane K., Egorov A., and Ivanov M. (1999) Chemical and isotopic evidence for the nature of the fluid in CH_4-containing sediments of the Hakon Mosby Mud Volcano. *Geo-Marine Lett.* **19**, 76–83.

Li Y-H., and Gregory S. (1974) Diffusion of ions in sea water and in deep-sea sediments. *Geochim. Cosmochim. Acta* **38**, 703–714.

Luff R., and Wallmann K. (2003) Fluid flow, methane fluxes, carbonate precipitation and biogeochemcial turnover in gas hydrate-bearing sediments at Hydrate Ridge, Cascadia Margin: numerical modeling and mass balances. *Geochim. Cosmochim. Acta* **67**, 3403–3421.

Lynch-Stieglitz J., Curry W. B., Oppo D. W., Ninneman U. S., Charles C. D., and Munson J. (2006) Meridional overturning circulation in the South Atlantic at the last glacial maximum. *Geochem. Geophys. Geosyst.* **7**(10), Q10N03. doi:10.1029/2005GC00122.

Mackensen A., Wollenburg J., and Licari L. (2006) Low $\delta^{13}C$ in tests of live epibenthic and endobenthic foraminifera at a site of active methane seepage. *Paleoceanography* **21**, PA2022. doi:10.1029/2005PA00119.

Mackenzie F. T., and Lerman A. (2006) *Carbon in the Geobiosphere—Earth's Outer Shell*. Springer-Verlag, Dordrecht, pp. 402.

Mackin J. E. (1986) The free-solution diffusion coefficient of boron: influence of dissolved organic matter. *Mar. Chem.* **20**, 131–140.

Marchitto T. M., Oppo D. W., and Curry W. B. (2002) Paired benthic foraminiferal Cd/Ca and Zn/Ca evidence for a greatly increased presence of Southern Ocean Water in the glacial North Atlantic. *Paleoceanography* **17**(3), 1038. doi:10.1029/2000PA00059.

Martin J. B., Day S. A., Rathburn A. E., Perez M. E., Mahn C., and Gieskes J. (2004) Relationships between the stable isotopic signatures of living and fossil foraminifera in Monterey Bay California. *Geochem. Geophys. Geosyst.* **5**(4), Q04004. doi:10.1029/2003GC000629.

Martin W. R., and Sayles F. L. (1996) CaCO$_3$ dissolution in sediments of the Ceara Rise, western equatorial Atlantic. *Geochim. Cosmochim. Acta* **60**(2), 243–263.

Masiello C. A., and Druffel E. R. M. (2003) Organic and black carbon ^{13}C and ^{14}C through the Santa Monica Basin sediment oxic-anoxic transition. *Geophys. Res. Lett.* **30**(4), 1185. doi:10.1029/2002GL015050.

Mayer L. A. (1991) Extraction of high-resolution carbonate data for palaeoclimate reconstruction. *Nature* **352**, 148–150.

McCorkle D. C., Emerson S. R., and Quay P. D. (1985) Stable carbon isotopes in marine porewaters. *Earth Planet Sci Lett* **74**, 13–26.

Meysman F. J. R., Middelburg J. J., Herman P. M. J., and Heip C. H. R. (2003) Reactive transport in surface sediments. II. Media: an object-oriented problem-solving environment for early diagenesis. *Compu. Geosci.* **29**, 301–318.

Morse J. W., and Mackenzie F. T. (1990) *Geochemistry of Sedimentary Carbonatesm.* , Vol. 48. Elsevier, Amsterdam.

O'Leary M. H. (1984) Measurement of the isotope fractionation associated with diffusion of carbon dioxide in aqueous solution. *J. Phys. Chem.* **88**, 823–825.

Press W. H., Flannery B. P., Teukolsky S. A., and Vetterling W. T. (1992) *Numerical Recipes in C: The Art of Scientific Computing.* Cambridge University, Cambridge, p. 1020.

Rathburn A. E., Perez M. E., Martin J. B., Day S. A., Mahn C., Gieskes J., Ziebis W., Williams D., and Bahls A. (2003) Relationships between the distribution and stable isotopic composition of living benthic foraminifera and cold methane seep biogeochemistry in Monterey Bay, California. *Geochem. Geophys. Geosyst.* **4**(12), 1106. doi:10.1029/2003GC000595.

Reimers C. E., Ruttenberg K. C., Canfield D. E., Christiansen M. B., and Martin J. B. (1996) Porewater pH and authigenic phases formed in the uppermost sediments of the Santa Barbara Basin. *Geochim. Cosmochim. Acta* **60**, 4037–4057.

Santschi P. H., Bower P., Nyffeler U. P., Azevedo A., and Broecker W. S. (1983) Estimates of the resistance to chemical transport posed by the deep-sea boundary layer. *Limnol. Oceanogr.* **28**, 899–912.

Sanyal A., Hemming N. G., Hanson G. N., and Broecker W. S. (1995) Evidence for a higher pH in the glacial ocean from boron isotopes in foraminifera. *Nature* **373**, 234–236.

Schaefer H., Whiticar M. J., Brook E. J., Petrenko V. V., Ferretti D. F., and Severinghaus J. P. (2006) Ice record of δ^{13}C for atmospheric CH$_4$ across the Younger Dryas-preboreal transition. *Science* **313**, 1109–1112.

Schimmelmann A., and Tegner M. J. (1991) Historical oceanographic events reflected in ^{13}C/^{12}C ratio of total organic carbon in laminated Santa Barbara Basin sediment. *Global Biogeochem. Cycles* **5**(2), 173–188.

Schink D. R. and Guinasso N. L. (1977) Modelling the influence of bioturbation and other processes on carbonate dissolution at the sea floor. In *The Fate of Fossil Fuel CO$_2$ in the Oceans* (eds. N. R. Anderson and A. Malahoff). Plenum Press, New York, pp. 375–399.

Sigman D. M., and Boyle E. A. (2000) Glacial/interglacial variations in atmospheric carbon dioxide. *Nature* **407**, 859–869.

Skinner L. C., and Shackleton N. J. (2005) An Atlantic lead over Pacific deep-water change across termination I: implications for the application of the marine isotope stage stratigraphy. *Quat. Sci. Rev.* **24**, 571–580.

Stott L. D., Bunn T., Prokopenko M., Mahn C., Giekes J., and Bernhard J. M. (2002) Does the oxidation of methane leave an isotopic fingerprint in the geologic record? *Geochem. Geophys. Geosyst.* **3**. doi:10.1029/2001GC000196.

Suess E., Torres M. E., Bohrmann G., Collier R. W., Greinert J., Linke P., Rehder G., Trehu A., Wallmann K., Winckler G., and Zuleger E. (1999) Gas hydrate destabilation: enhanced dewatering, benthic material turnover and large methane plumes at the Cascadia convergent margin. *Earth Planet. Sci. Lett.* **170**, 1–15.

Sundquist E. T. (1986) Geologic analogs: their value and limitations in carbon dioxide research. In *The Changing Carbon Cycle: A Global Analysis* (eds. J. R. Trabalka and D. E. Reichle). Springer-Verlag, New York, pp. 371–402.

Torres M. E., Mix A. C., Kinports K., Haley B., Klinkhammer G. P., McManus J., and de Angelis M. A. (2003) Is methane venting at the seafloor recorded by δ^{13}C of benthic foraminifera shells? *Paleoceanography* **18**(3). doi:10.1029/2002PA000824.

Torres M. E., Wallmann K., Tréhu A. M., Bohrmann G., Borowski W. S., and Tomaru H. (2004) Gas hydrate growth, methane transport, and chloride enrichment at the southern summit of Hydrate Ridge, Cascadia margin off Oregon. *Earth Planet. Sci. Lett.* **226**, 225–241.

Tyrrell T., and Zeebe R. E. (2004) History of carbonate ion concentration over the last 100 million years. *Geochim. Cosmochim. Acta* **68**(17), 3521–3530.

Van Cappellen P., and Wang Y. (1996) Cycling of iron and manganese in surface sediments: a general theory for the coupled transport and reaction of carbon, oxygen, nitrogen, sulfur, iron, and manganese. *Am. J. Sci.* **296**, 197–243.

Wallmann K., Linke P., Suess E., Bohrmann G., Sahling H., Schlüter M., Dählmann A., Lammers S., Greinert J., and von Mirbach N. (1997) Quantifying fluid flow, solute mixing, and biogeochemical turnover at cold vents of the eastern Aleutian subduction zone, *Geochim. Cosmochim. Acta* **61**(24), 5209–5219.

Wolf-Gladrow D. A., Bijma J., and Zeebe R. E. (1999) Model simulation of the carbonate system in the microenvironment of symbiont bearing foraminifera. *Mar. Chem.* **64**, 181–198.

Wolf-Gladrow D. A., Zeebe R. E., Klaas C. Körtzinger A., and Dickson A. G. (in press) Total alkalinity: the explicit conservative expression and its application to biogeochemical processes, *Mar. Chem.* doi: 10.1016/j.marchem.2007.01.006.

Yu J., and Elderfield H. (2006) The role of the seawater carbonate system on trace element partition into foraminiferal calcium carbonate based on field and paleoproxy studies. *Eos Trans AGU* **87**(52), Fall Meet. Suppl., Abstract B21D–05.

Zeebe R. E., Sanyal A., Ortiz J. D., and Wolf-Gladrow D. A. (2001) A theoretical study of the kinetics of the boric acid–borate equilibrium in seawater. *Mar. Chem.* **74**(2), 113–124.

Zeebe R. E., and Sanyal A. (2002) Comparison of two potential strategies of planktonic foraminifera for house building: Mg^{2+} or H$^+$ removal? *Geochim. Cosmochim. Acta* **66**(7), 1159–1169.

Zeebe R. E., and Wolf-Gladrow D. A. (2001) *CO$_2$ in Seawater: Equilibrium, Kinetics, Isotopes.* Elsevier Oceanography Series, Amsterdam, pp. 346.

Zeebe, R. E. and Zachos J. C. (in press) Reversed deep-sea carbonate ion basin-gradient during Paleocene–Eocene

Thermal Maximum. *Paleoceanography*. doi: 10.1029/2006PA001395.

Zeebe R. E., Wolf-Gladrow D. A., Bijma J., and Hönisch B. (2003) Vital effects in planktonic foraminifera do not compromise the use of $\delta^{11}B$ as a paleo-pH indicator: evidence from modeling. *Paleoceanography* **18**(2), 1043. doi:10.1029/2003PA000881.

Zeebe R. E., Bijma J., and Wolf-Gladrow D. A. (1999a) A diffusion-reaction model of carbon isotope fractionation in foraminifera. *Mar. Chem.* **64**, 199–227.

Zeebe R. E., Jansen H., and Wolf-Gladrow D. A. (1999b) On the time required to establish chemical and isotopic equilibrium in the carbon dioxide system in seawater. *Mar. Chem.* **65**, 135–153.

Zhang J., Quay P. D., and Wilbur D. O. (1995) Carbon isotope fractionation during gas-water exchange and dissolution of CO_2. *Geochim. Cosmochim. Acta* **59**, 107–114.

Associate editor: John W. Morse